J. Fluid Mech. (2010), *vol.* 655, *pp.* 380–418.
doi:10.1017/S0022112010000960

Spatial structure of a turbulent boundary layer with irregular surface roughness

Y. WU† AND K. T. CHRISTENSEN‡

Department of Mechanical Science and Engineering, University of Illinois, Urbana, IL 61801, USA

(Received 20 November 2009; revised 18 February 2010; accepted 18 February 2010; first published online 19 May 2010)

Particle image velocimetry experiments were performed to study the impact of realistic roughness on the spatial structure of wall turbulence at moderate Reynolds number. This roughness was replicated from an actual turbine blade damaged by deposition of foreign materials and its features are quite distinct from most roughness characterizations previously considered as it is highly irregular and embodies a broad range of topographical scales. The spatial structure of flow over this rough surface near the outer edge of the roughness sublayer is contrasted with that of smooth-wall flow to identify any structural modifications due to roughness. Hairpin vortex packets are observed in the outer layer of the rough-wall flow and are found to contribute heavily to the Reynolds shear stress, consistent with smooth-wall flow. While similar qualitative consistency is observed in comparisons of smooth- and rough-wall two-point correlations, some quantitative differences are also apparent. In particular, a reduction in the streamwise extent of two-point correlations of streamwise velocity is noted which could be indicative of a roughness-induced modification of outer-layer vortex organization. Proper orthogonal decomposition analysis reveals the streamwise coherence of the larger scales to be most sensitive to roughness while the spatial characteristics of the smaller scales appear relatively insensitive to such effects.

1. Introduction

Much has been uncovered regarding the outer-layer structure of smooth-wall turbulence (Robinson 1991; Panton 1997). In particular, it is well documented that hairpin-like vortices populate the outer region at low and moderate Reynolds numbers (Re) and align coherently to form larger-scale structures termed hairpin vortex packets (Head & Bandyopadhyay 1981; Smith 1984; Smith *et al.* 1991; Zhou *et al.* 1999; Adrian, Meinhart & Tomkins 2000*b*; Christensen & Adrian 2001; Ganapathisubramani, Longmire & Marusic 2003; Tomkins & Adrian 2003; Delo, Kelso & Smits 2004). These coherent trains of vortices collectively induce strong ejections of fluid away from the wall which contribute heavily to the mean Reynolds shear stress (RSS), $\langle u'v' \rangle$ (Ganapathisubramani *et al.* 2003). In the streamwise–wall-normal plane these large-scale structures appear as inclined interfaces formed by streamwise-aligned spanwise vortex cores beneath which a region of relatively uniform low-momentum fluid resides due to the collective induction of the vortices in the packet. In the streamwise–spanwise plane hairpin packets appear as elongated

† Present address: Department of Mechanical and Materials Engineering, Wright State University, Dayton, OH 45435, USA

‡ Email address for correspondence: ktc@illinois.edu

low-momentum regions (LMRs) that are bounded by wall-normal vortex cores associated with the legs/necks of the individual vortices and within which intense ejections of low-speed fluid occur. Previous studies have established that these vortex packets play a pivotal role in momentum and energy transport in smooth-wall flow (Chong *et al.* 1998; Kim & Adrian 1999; Guala, Hommema & Adrian 2006; Natrajan & Christensen 2006; Balakumar & Adrian 2007) and recent experiments indicate that LMRs observed in δ-scale PIV studies may be a part of much longer 'superstructures' that can extend several δ in the streamwise direction and meander significantly in the spanwise direction (Hutchins & Marusic 2007). In addition, these large-scale structures leave their imprint on the spatial correlations of smooth-wall flow (Christensen & Adrian 2001; Tomkins & Adrian 2003; Ganapathisubramani *et al.* 2005; Christensen & Wu 2005). For example, the streamwise extent and inclination angle of the two-point correlation coefficient of streamwise velocity (ρ_{uu}) in the streamwise–wall-normal plane are both consistent with the spatial characteristics of hairpin vortex packets. In contrast, the spatial extent of the two-point correlation of wall-normal velocity (ρ_{vv}) is comparable to the spatial extent of the heads of hairpin-like structures. These imprints provide an excellent measure of the average characteristics of such structures as well as a glimpse of their persistence and organizational consistency.

The impact of roughness on this structural paradigm of smooth-wall turbulence is still a topic of intense interest as any alteration of its characteristics may significantly impact on how one models momentum and energy transport in such flows. Several studies have considered this issue, but for rather idealized surface conditions (sand grain, wire mesh, ordered arrays of elements, etc.). Krogstad & Antonia (1994), for example, computed two-point velocity correlations from cross-wire measurements and found that the inclination angle of ρ_{uu} increased to approximately 38° for flow over a mesh surface ($\delta/k \approx 50$, $\delta/k_s \approx 15$, $k^+ = 92$, $k_s^+ = 331$, where k is the geometric height of the roughness and k_s is the equivalent sand-grain height) compared to the smooth-wall angle of 10°–15° observed in many studies (Brown & Thomas 1977; Christensen & Adrian 2001; Christensen & Wu 2005). In addition, they reported a dramatic decrease in the streamwise extent of velocity and vorticity correlations compared to flow over a smooth wall that persisted well into the outer layer but found little difference in the spanwise extent of these correlations. While weaker streamwise shortening of velocity correlations has been observed in other studies of rough-wall turbulence (Raupach, Antonia & Rajagopalan 1991; Wu & Christensen 2007; Volino, Schultz & Flack 2007), these efforts also reported this shortening to diminish significantly with increasing distance from the wall and eventual consistency with smooth-wall flow outside the roughness sublayer. Such outer-layer similarity is in accordance with Townsend's wall similarity hypothesis which conjectures that surface conditions set the wall shear stress (and hence the friction velocity, $u_\tau \equiv \sqrt{\tau_w/\rho}$) and the boundary-layer thickness, δ, while the outer-layer turbulence simply adjusts to such conditions in a universal manner. A necessary condition for such similarity to exist in rough-wall turbulence appears to be significant scale separation between the outer length scale of the flow (δ) and the characteristic height of the roughness (taken as either k or k_s). Jimenez (2004) suggests $\delta/k \gtrsim 50$ for such similarity to exist, while Flack, Schultz & Shapiro (2005) proposes $\delta/k_s \gtrsim 40$. Indeed, many rough-wall turbulence studies exhibit such similarity in the single-point statistics, both for flow over idealized surfaces (Raupach 1981; Ligrani & Moffat 1986; Bandyopadhyay & Watson 1988; Bakken *et al.* 2005; Flack *et al.* 2005; Kunkel & Marusic 2006, among others) as well as for flow over more irregular topographies (Allen *et al.* 2007; Wu &

Christensen 2007). In contrast, other studies report single-point statistics affected by roughness well into the outer layer (Krogstad, Antonia & Browne 1992; Krogstad & Antonia 1999; Keirsbulck *et al.* 2002; Tachie, Bergstrom & Balachandar 2000, 2003). However, most of these efforts had weak scale separation between the roughness and the outer length scale of the flow, yielding δ/k and/or δ/k_s values well below the thresholds proposed by Jimenez (2004) and Flack *et al.* (2005).

Nakagawa & Hanratty (2001) reported two-point streamwise velocity correlation coefficients computed from ensembles of instantaneous velocity fields acquired by particle image velocimetry (PIV) in channel flow with a wavy bottom wall ($\delta/k \approx 60$) and found that neither their length scale nor their inclination angle were altered in the presence of the wavy surface. Sabot, Saleh & Comte-Bellot (1977) studied pipe flow roughened with spanwise fences ($\delta/k = 15$) and found the streamwise integral length scales of the streamwise and wall-normal velocities to change little from smooth-wall pipe flow. More recently, Volino *et al.* (2007) concluded that the outer-layer structure of flow over a fully-rough woven mesh ($\delta/k = 71$) was similar to that observed in smooth-wall flow via comparison of velocity spectra and two-point correlations, though a reduction in streamwise extent of ρ_{uu} by roughness was noted within the roughness sublayer. Similar structural consistencies in the outer layer were also observed in a recent direct numerical simulation (DNS) of channel flow with disturbed walls by Flores, Jimenez & del Alamo (2007). In contrast, Volino, Schultz & Flack (2009) found the outer-layer structure of a turbulent boundary layer to be more affected by two-dimensional roughness ($\delta/k = 32$). It was concluded that this roughness generates flow structures much larger than k due to the width of the roughness and that the growth of these motions into the outer layer enhanced the turbulent stresses and the integral length scales. These observations highlight the fundamental differences between flow over three-dimensional and two-dimensional roughness as other studies of two-dimensional roughness have similarly reported strong outer-layer modifications in an external flow arrangement (Krogstad & Antonia 1999; Keirsbulck *et al.* 2002; Lee & Sung 2007).

While the many studies cited above document the impact of sand grain, k- or d-type transverse bars, wire mesh and ordered arrays of elements on turbulence structure, these topographies are highly idealized since they often contain a single roughness scale arranged in an ordered manner. In contrast, the roughness encountered in a variety of practical applications, such as that of damaged turbine-blade surfaces (Bons *et al.* 2001) and the surfaces of ships and submarines (Karlsson 1980), can be highly irregular and contain a broad range of topographical scales. In the case of turbine blades, surface roughness is attributable to multiple damage mechanisms, including pitting/erosion, spallation and/or deposition of foreign materials (Bons *et al.* 2001). Given the complex nature of these practical topographies, it is not clear whether studies of idealized roughness are sufficient for accurately characterizing the turbulent physics in the presence of more practical roughness. Differences in friction factor in the transitionally rough regime for realistic and idealized roughness have been well known since Nikuradse's results for sand-grain roughness (Nikuradse 1933) and Colebrook's relationship based on 'industrial' roughness (Colebrook 1939). Bons (2002) also found that traditional rough-wall correlations for heat transfer and skin friction severely under-predicted such behaviour for turbulent flow over turbine-blade roughness, particularly in the transitionally rough regime.

The impact of more realistic roughness on the character of turbulence has received renewed attention recently, and evidence exists supporting outer-layer similarity in the single-point turbulence statistics in the presence of such highly three-dimensional

surfaces. For example, Allen *et al.* (2007) reported strong consistency in the streamwise Reynolds normal stresses and streamwise velocity spectra in the outer layer for flow through a pipe roughened by the honing process ($\delta/k \sim 51\,000$, $\delta/k_s \sim 17\,000$). In addition, Wu & Christensen (2007) recently reported excellent agreement between the single-point turbulence statistics (streamwise and wall-normal Reynolds normal stresses, RSS, contributions to RSS by various quadrant events, etc.) in the outer layer between flow over a surface replicated from a turbine blade damaged by deposition of foreign materials ($\delta/k = 27$, $\delta/k_s = 48$) and smooth-wall flow.

The present effort is devoted to a comparison of the structural character of turbulent flow over the highly irregular surface topography reported in Wu & Christensen (2007) with that of smooth-wall turbulence. PIV measurements were performed in both the streamwise–wall-normal (x–y) and the streamwise–spanwise (x–z) plane at $y = 0.15\delta$. The spatial characteristics of velocity and swirling-strength correlations are then explored as a means of identifying modifications of the underlying spatial structure due to roughness. Proper orthogonal decomposition (POD) is then used to explore these possible modifications further.

2. Experiments

Both two-dimensional and stereoscopic PIV were used to study the impact of surface roughness replicated from a turbine blade damaged by deposition of foreign materials on a zero-pressure-gradient turbulent boundary layer at $Re_\theta \equiv U_e\theta/\nu \approx 13\,000$, where U_e is the free-stream velocity, θ is the momentum thickness and ν is the kinematic viscosity of the fluid. While the curvature of turbine blades imposes significant pressure-gradient effects in practice, zero-pressure-gradient conditions were studied herein to isolate the impact of irregular roughness on the flow. All measurements were made in an Eiffel-type, open circuit, boundary-layer wind tunnel with a documented turbulence intensity of 0.16 % in the free stream (Meinhart 1994). The working section of the tunnel is 6.1 m long, 0.91 m wide and 0.46 m tall within which a 6 m long hydraulically smooth flat plate with an elliptically shaped leading edge is suspended 100 mm above the floor of the tunnel. This boundary-layer surface consists of two separate 3 m long by 0.91 m wide flat plates smoothly joined at the streamwise centre. Zero-pressure-gradient conditions within 1 % of the free-stream dynamic head were achieved for both surface conditions through fine adjustment of the test-section ceiling height along its length. Fluid properties were assessed from measurements of the atmospheric pressure and air temperature using an ideal gas relation in concert with Sutherland's correlation for kinematic viscosity. The characteristics of this tunnel have been documented in many past studies (Meinhart & Adrian 1995; Adrian *et al.* 2000*b*; Tomkins & Adrian 2003; Wu & Christensen 2006, 2007; Balakumar & Adrian 2007; Natrajan, Wu & Christensen 2007).

2.1. *Rough surface*

The surface under consideration was derived from a surface profilometry scan of a turbine blade damaged by deposition of foreign materials reported by Bons *et al.* (2001) and used by Bons (2002) to study bulk skin friction and heat transfer characteristics over turbine-blade roughness. As discussed in Wu & Christensen (2007), in order to generate appropriate roughness conditions for the relatively thick boundary layers under study ($\delta = 102$ mm and 112 mm for the smooth- and rough-wall cases, respectively) the original topographical information was scaled up in all three dimensions to yield an average peak-to-valley roughness height of $k = 4.2$ mm.

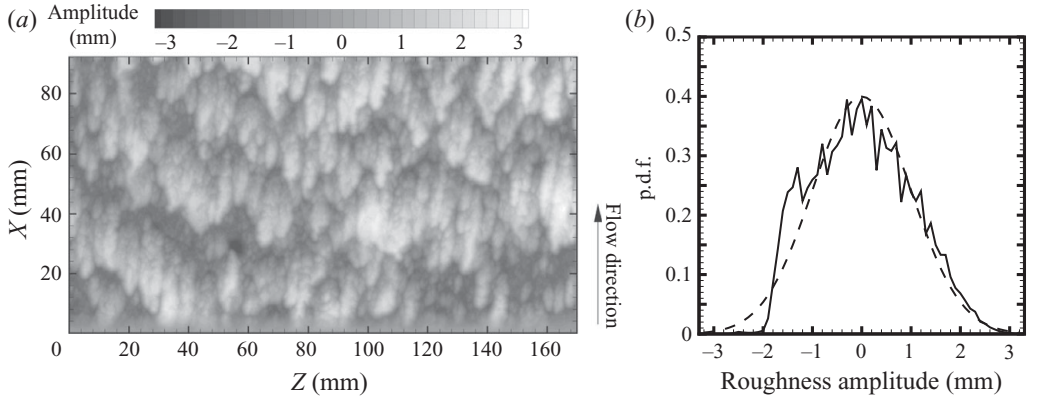

FIGURE 1. (*a*) Topographical map of a portion of the roughness considered herein. (*b*) Probability density function (p.d.f.) of roughness amplitude about the mean elevation (——) contrasted with a Gaussian distribution with an equivalent RMS (– – –).

At this scaling, the root-mean-square (RMS) roughness height, k_{rms}, is 1.0 mm while the skewness and flatness are 0.19 and 2.35, respectively. This surface condition was referred to as the 'RF1' surface condition in Wu & Christensen (2007) and yields a ratio of the boundary-layer thickness to the characteristic roughness height of $\delta/k = 27$.

Figure 1(*a*) presents a topographical map of a portion of this roughness topography. The dominant topographical features of this surface are elliptical in shape and are generally aligned in the streamwise direction. However, a broad range of topographical scales is also clearly evident, rendering the surface quite irregular compared to idealized roughness characterizations (wire mesh, arrays of cylinders of hemispheres, etc.). In this regard, while such idealized characterizations are typically marked by a specific roughness element size often arranged in an ordered manner, the present rough surface has elements that vary appreciably in both size, shape and spacing and hence is termed irregular in character. Such deposits are typically observed on the trailing edge of the pressure surfaces of land-based turbine blades, like that profiled by Bons *et al.* (2001), and such deposits are known to severely degrade blade performance. Figure 1(*b*) presents the probability density function (p.d.f.) of the fluctuating roughness amplitude contrasted with a Gaussian distribution with an equivalent RMS. This p.d.f. highlights the broad range of topographical fluctuations that exist about the mean elevation but, as the aforementioned flatness value of 2.35 suggests, the p.d.f. of the roughness amplitude is not strictly Gaussian. As discussed in Wu & Christensen (2007), a three-dimensional powder-deposition printer was used to construct replicas of the topography. The downstream 3 m (equivalently $\sim 30\delta$) of the boundary-layer plate in the wind tunnel was covered with roughness to ensure self-similar conditions at the measurement location. Thus, since the original spatial footprint of the digitized topography was not sufficient to fill this large an area, the topography was mirrored in both the streamwise and spanwise directions to achieve an appropriate streamwise fetch of roughness. The resulting 25 cm $\times$ 30 cm roughness panels were carefully mounted to cast aluminium plates with a spray adhesive which yielded an elevation uncertainty of not more than $\pm 25\,\mu$m from panel to panel (Wu & Christensen 2007). To accommodate these panels in the wind tunnel, the boundary-layer plate was separated into two at its streamwise centre and the upstream half was raised relative to the downstream half such that the mean elevation of the

Surface	Re_θ	U_e	δ	u_τ	δ^+	ΔU^+	k	k^+	k_s^+	δ/k	δ/k_s	$5k/\delta$	Δ^+
–	–	(m s^{-1})	(mm)	(m s^{-1})	–	–	(mm)	–	–	–	–	–	–
Smooth	11940	16.2	104	0.53	3470	–	–	–	–	–	–	–	19
Rough	14780	16.9	112	0.76	5530	8.2	4.2	207	115	27	48	0.188	18

TABLE 1. Summary of experimental parameters.

roughness was coincident with the upstream smooth wall. The aluminium plates containing the roughness were then laid along the downstream half of the boundary-layer plate in the wind tunnel. Both the smooth- and rough-wall flows were tripped with a cylindrical rod 5.5 m upstream of the measurement location and measurements were conducted at similar Re_θ.

2.2. *Two-dimensional PIV measurements in the streamwise–wall-normal plane*

Two-dimensional PIV measurements were first performed in the streamwise–wall-normal (x–y) plane at the spanwise centre of the test section for smooth- and rough-wall flow (at the spanwise centre of a single roughness tile), with details reported in Wu & Christensen (2007). The flow field was illuminated through a transparent section in the wind-tunnel ceiling with a 500 μm thick laser sheet generated by a pair of Nd:YAG lasers (190 mJ pulse^{-1}). The flow was seeded with 1 μm olive oil droplets generated by a Laskin nozzle and time-separated images of the scattered light from the particles were captured with a $4k \times 2.8k$, 12-bit frame-straddle CCD camera over a field of view of $1.4\delta \times \delta$ (streamwise by wall-normal). The measurements over both smooth and rough walls were performed 5.55 m downstream of the leading edge of the flat plate (equivalently 2.5 m downstream of the leading edge of the roughness). The roughness in the vicinity of the measurement location was spray-painted black to reduce reflections of laser light; however, the remaining unsuppressed reflections prevented measurements in the region $y < 0.08\delta$ for the rough-wall case. Flow parameters are summarized in table 1.

The pairs of PIV images were interrogated using a recursive two-frame cross-correlation method (Wu & Christensen 2007). The sizes of the interrogation windows were chosen to maintain a consistent vector grid spacing of $\Delta x^+ = \Delta y^+ = \Delta^+ \approx 18$ between the smooth- and rough-wall data when scaled in inner units (by u_τ and ν). The resulting velocity vector fields were then validated to remove erroneous vectors with a 95 %–97 % valid vector yield achieved, minimizing the need for interpolation of holes. Each velocity field was then low-pass filtered to remove noise associated with frequencies larger than the sampling frequency of the interrogation. The uncertainty in instantaneous velocity was estimated to be approximately 1 % (see Wu & Christensen (2007) for further details).

As discussed in Wu & Christensen (2007), u_τ for each case was determined using the total shear stress method which assumes a region of constant total shear stress equal to the wall shear stress in the overlap and inner region of the boundary layer (Flack *et al.* 2005). As such, the friction velocity was deduced from the measured mean velocity and RSS profiles with an uncertainty of approximately 6 % (Wu & Christensen 2007). Values of u_τ estimated in this manner were then used to determine the virtual origin $y_\circ$ and the roughness function ΔU^+ for the rough-wall cases by fitting the mean velocity profile to the expected logarithmic profile in the log layer.

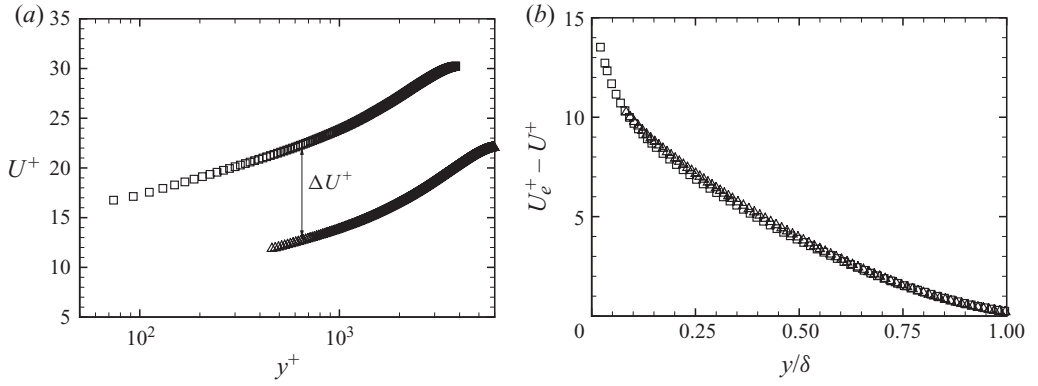

FIGURE 2. Mean velocity profiles in (*a*) inner and (*b*) velocity defect scalings. Not all data points shown for clarity. □: smooth; △: rough.

Figure 2 presents mean velocity profiles for the smooth- and rough-wall cases in inner and velocity defect scalings. These profiles were computed by ensemble-averaging the velocity fields for a given case followed by line-averaging in the streamwise direction (Wu & Christensen 2007). The presence of roughness shifts the logarithmic region of the mean velocity profile downwards by $\Delta U^+ = 8.2$ and enhances the friction velocity by 43 % relative to the smooth-wall baseline (see table 1). Given $\Delta U^+ = 8.2$ for the rough-wall case, an equivalent sand-grain height of $k_s^+ = 115$ was determined which places it well within the fully rough regime based on accepted historical classifications (Nikuradse 1933). In addition, while $\delta/k = 27$ which is below the criterion of $\delta/k \gtrsim 50$ proposed by Jimenez (2004) for the existence of wall similarity, $\delta/k_s = 48$ which satisfies the alternative criterion of Flack *et al.* (2005) ($\delta/k_s \gtrsim 40$). Interestingly, excellent agreement is noted between the smooth- and rough-wall mean velocity profiles in the overlap and outer layers in velocity defect scaling (figure 2*b*). This agreement indicates that roughness effects on the mean velocity are confined to the inner layer of the rough-wall flow, supporting the existence of outer-layer similarity. Similar collapse of smooth- and rough-wall mean velocity profiles in defect scaling was also noted recently by Connelly, Schultz & Flack (2006) for turbulent boundary layers in the presence of sand grains and wire mesh as well as by Allen *et al.* (2007) for honed surfaces in turbulent pipe flow. Finally, as previously reported in Wu & Christensen (2007), the single-point statistics for the present smooth- and rough-wall cases ($\langle u'^2\rangle^+$, $\langle v'^2\rangle^+$ and $\langle u'v'\rangle^+$) as well as RSS contributions as assessed by quadrant analysis collapsed for $y \gtrsim 5k$ in accordance with Townsend's wall similarity hypothesis.

2.3. *Stereo PIV measurements in the streamwise–spanwise plane*

Stereo PIV measurements were also performed in the streamwise–spanwise (x–z) plane at $y = 0.15\delta$ of both flows (relative to the virtual origin for the rough-wall case). This wall-normal location was selected because $y = 0.15\delta = 4k$ is near the outer edge of the roughness sublayer for the rough-wall case. To facilitate these measurements, a second $4k \times 2.8k$, 12-bit frame-straddle CCD camera was added to the aforementioned camera and laser system. The two CCD cameras viewed the flow through a transparent section in the wind-tunnel ceiling and their imaging paths were rotated at an angle of $\theta = \pm 15^\circ$ with respect to the wall-normal (y) axis. The laser light sheets were formed in a manner identical to that described earlier but were introduced into the tunnel through a glass sidewall while their orientations were carefully adjusted to ensure

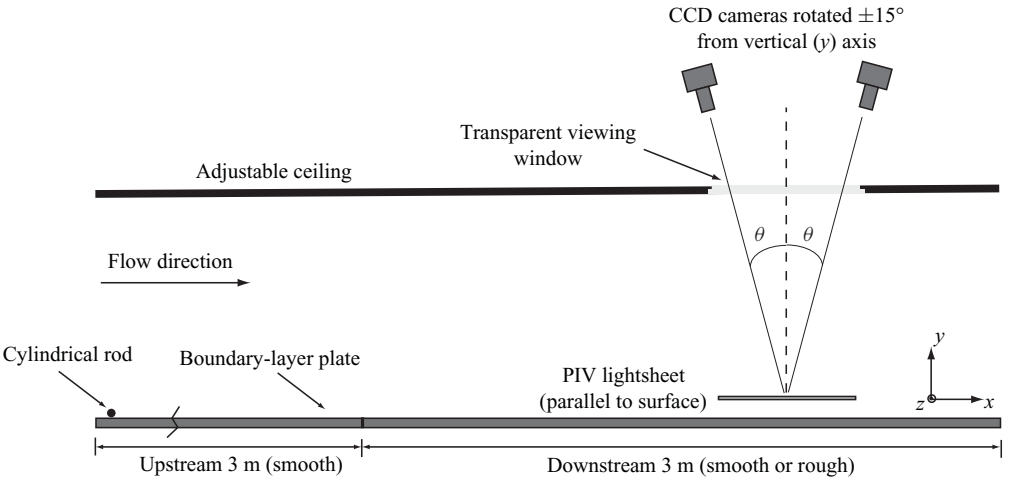

FIGURE 3. Side view of experimental arrangement for stereo PIV measurements in the streamwise–spanwise plane.

they remained parallel to the wall at $y = 0.15\delta$. Uniform image focus was ensured in both cameras across the entire field of view by satisfying the Scheimpflug condition. Figure 3 presents a side view of the experimental arrangement for the stereo PIV measurements.

The pairs of images acquired by each camera were interrogated and validated independently in accordance with the methodology described in § 2.2, yielding pairs of instantaneous planar fields of two-dimensional particle displacements from the two distinct views of the measurement plane. Each pair of two-dimensional displacement fields was then reconstructed into a single, three-component instantaneous velocity field via calibration of the imaging system. First proposed by Soloff, Adrian & Liu (1997), this *in situ* three-dimensional calibration method requires no knowledge of the system geometry and it accounts for optical distortions that might exist along the viewing path of the imaging system. A mapping function from the image plane to the measurement plane was constructed using images of a calibration target at different depth locations within the laser light sheet acquired by both cameras. A dual-plane (1 mm separation) target of white dots spaced at in-plane intervals of 10 mm over a 20 cm × 20 cm region was employed, alleviating the need to physically translate the target through the thickness of the light sheet. The mapping function was further optimized using the self-calibration scheme proposed by Wieneke (2005) to reduce registration errors associated with inherent misalignment of the calibration target with the laser light sheet. The final mapping function was then used to reconstruct three-dimensional velocity vectors on the measurement plane from the pairs of two-dimensional particle displacements with vector grid spacings that matched those of the x–y PIV measurements. The uncertainty in instantaneous velocity for the in-plane components of this stereo PIV data is comparable to that of the two-dimensional PIV measurements (approximately 1 %) while the uncertainty in out-of-plane velocity is approximately twice this based on previous studies (Soloff *et al.* 1997). Twenty-five hundred statistically independent fields were acquired for each case. Of particular importance, the flow conditions for the x–y plane experiments were replicated to within less than 1 % of U_e for these wall-parallel measurements to ensure consistency between the data sets.

3. Instantaneous structure

Instantaneous velocity fields in both the x–y and x–z planes are used to discern whether the instantaneous structure of smooth-wall turbulence in the outer layer is appreciably altered in the presence of the rough surface considered herein. In this regard, since $k^+ = 207$ and $k_s^+ = 115$ it is clear that roughness has some direct impact on the flow at the lower edge of the logarithmic region. Further, given that $5k/\delta = 0.188$ and $5k_s/\delta = 0.1$ (two different measures of the outer edge of the roughness sublayer), it is likely that such an impact extends well into the logarithmic region.

3.1. *Smooth-wall flow*

Figure 4(a) presents a representative instantaneous velocity realization of smooth-wall flow acquired in the streamwise–wall-normal (x–y) plane and visualized with a constant advection velocity of $0.77U_e$ removed. Consistent with previous observations of hairpin vortex packets in wall turbulence (Adrian *et al.* 2000*b*; Christensen & Adrian 2001), several swirling motions with clockwise rotation (hairpin heads) appear aligned in the streamwise direction and form a large-scale interface inclined slightly away from the wall beneath which exists a large-scale region of streamwise momentum deficit mutually-induced by the vortices in the packet. As a part of this induction, each vortex generates a strong ejection of low-momentum fluid away from the wall just upstream and below its head and these ejection events contribute significantly to the overall RSS. The strength of these ejection events is quite evident in figure 4(b) which presents contours of instantaneous inner-scaled $u'v'$ computed from the fluctuating velocity field associated with figure 4(a). Line contours of $u = 0.77U_e$ (the advection velocity removed) are overlaid on this field to aid in demarcating the inclined interface of the hairpin packet. Finally, the level of vortical activity present in this instantaneous realization can be seen in figure 4(c) which presents contours of a vortex identifier termed swirling strength (Zhou *et al.* 1999; Adrian, Christensen & Liu 2000*a*), λ_{ci}, weighted with the sign of the instantaneous fluctuating spanwise vorticity, ω_z, to distinguish between prograde (negative ω_z; clockwise) and retrograde (positive ω_z; counter-clockwise) spanwise vortices. Several negative patches of λ_{ci} are evident along the inclined interface of the low-momentum region and are interpreted as the λ_{ci} signatures of the hairpin vortex heads. Although less numerous, several retrograde spanwise vortices exist and Wu & Christensen (2006) reported these structures to occur most frequently near the outer edge of the log layer where they often occur in close proximity to prograde vortices. Natrajan *et al.* (2007) found that spatially-coincident prograde and retrograde spanwise vortices may be linked to an x–y PIV measurement plane slicing through the shoulders of omega-shaped hairpin-like structures.

Outer-layer vortex organization also leaves a definitive imprint in wall-parallel (x–z) velocity fields within the log layer of smooth-wall turbulence. Figure 5(a) presents a representative instantaneous fluctuating velocity field of smooth-wall flow in the wall-parallel plane at $y = 0.15\delta$. The in-plane fluctuating velocity components (u', w') are shown as vectors while the out-of-plane v' component is presented as background contours. Two large-scale events are notable in this field: an elongated low-momentum region ($u' < 0$; labelled 'LMR') and an elongated high-momentum region ($u' > 0$; labelled 'HMR'). Both of these events have spanwise widths of 0.2δ–0.3δ and are quite consistent with previous observations of such regions in the log layer of smooth-wall turbulence (see e.g. Ganapathisubramani *et al.* 2003; Tomkins & Adrian 2003; Ganapathisubramani *et al.* 2005). Numerous swirling motions are noted along the boundaries of these elongated regions as are intense ejections of fluid away from the wall ($v' > 0$) within the LMR and sweeps of fluid

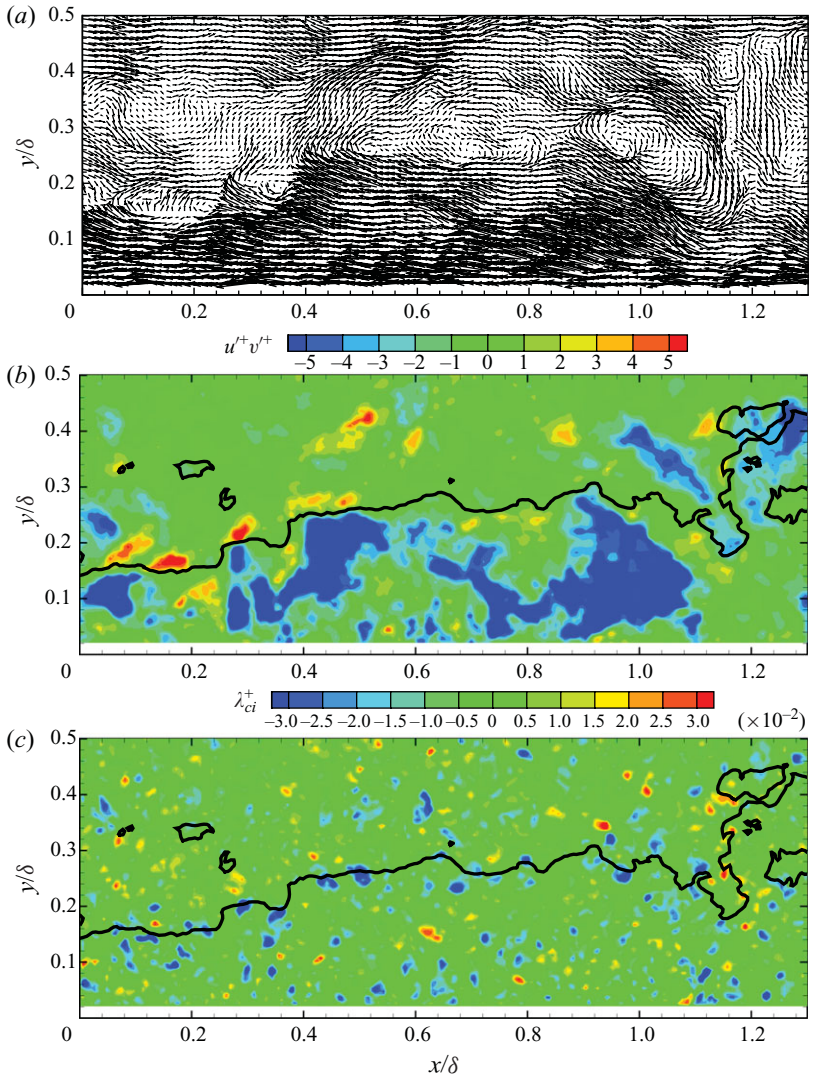

FIGURE 4. A representative instantaneous velocity realization in the streamwise–wall-normal plane of smooth-wall flow. (*a*) Galilean decomposition with a constant streamwise advection velocity of $0.77U_e$ removed. (*b*) Instantaneous contributions to RSS, $u'v'$. (*c*) Instantaneous swirling strength, λ_{ci}. Line contours outlining low-momentum interface (with $0.77U_e$ threshold) overlaid in (*b*) and (*c*).

towards the wall ($v' < 0$) within the HMR. The spatial imprints of the LMR and HMR are quite evident in figure 5(*b*) which presents contours of instantaneous streamwise velocity u normalized by the ensemble- and area-averaged mean velocity U. These elongated regions of relatively constant streamwise momentum extend the entire field of view ($\sim 0.8\delta$) in the streamwise direction and, while they are generally aligned in the streamwise direction, they also tend to meander in the spanwise direction. Figure 5(*c*) presents inner-scaled $u'v'$ contours computed from the instantaneous velocity field in figure 5(*a*) with line contours outlining the low- (white) and high-momentum (black) regions using thresholds of $u = 0.85U$ and $1.15U$, respectively. Of significance, the most intense $u'v'$ events occur within the LMR and

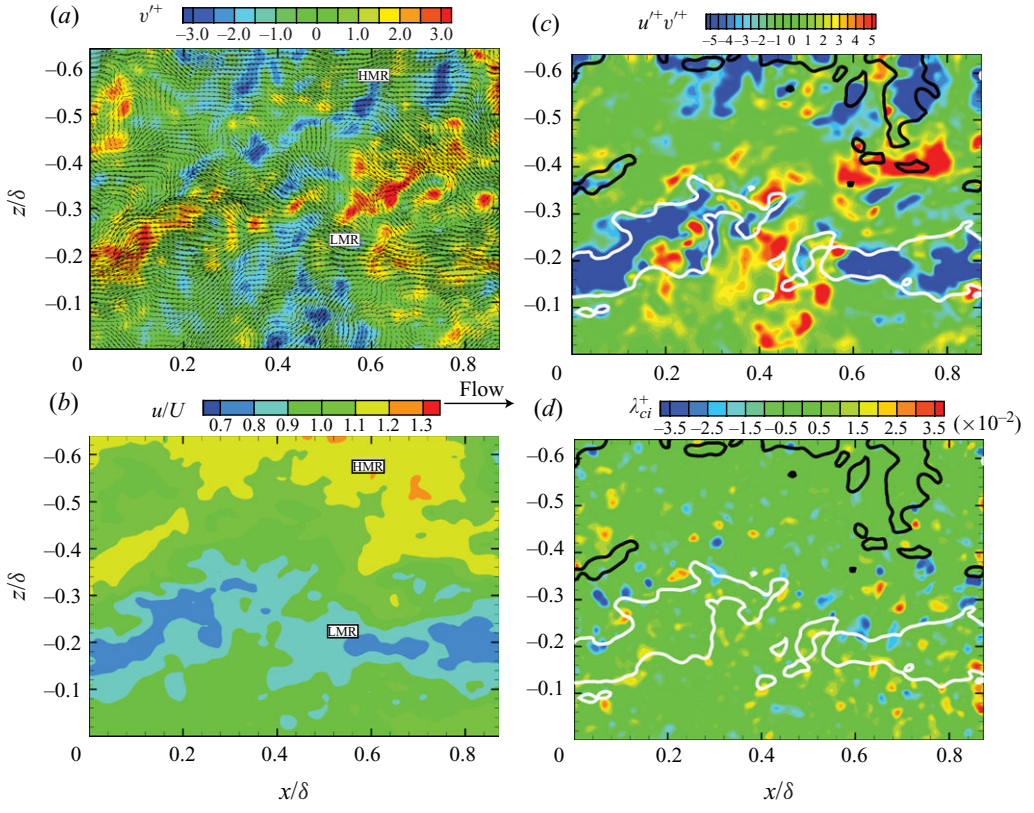

FIGURE 5. A representative instantaneous velocity realization in the streamwise–spanwise plane at $y = 0.15\delta$ for smooth-wall flow. (*a*) Fluctuating in-plane velocities (u', w') are presented as vectors and the fluctuating out-of-plane velocity v' is presented as contours. (*b*) Contours of normalized streamwise velocity, u/U. (*c*) Instantaneous contributions to RSS, $u'v'$. (*d*) Instantaneous swirling strength, λ_{ci}. Line contours of low- (white; $0.85U$) and high-momentum (black; $1.15U$) regions are presented in the background.

HMR. Finally, the wall-normal swirling motions outboard of the LMR and HMR can be visualized in figure 5(*d*) which presents contours of λ_{ci} for this velocity realization. Opposing-sign λ_{ci} is noted along the spanwise boundaries of these regions. As noted previously by Tomkins & Adrian (2003) and Ganapathisubramani *et al.* (2003), the LMR bounded by swirling motions and within which intense $u'v'$ events are noted is consistent with what one would observe if a streamwise-aligned hairpin vortex packet were sliced in a wall-parallel plane. In contrast, the HMR can be interpreted as a region of relatively high-momentum fluid formed outboard of the hairpin packets due to the collective induction of the vortices which sweep high-momentum fluid towards the wall that also contributes heavily to the overall RSS (figure 5*c*). Finally, recent observations by Hutchins & Marusic (2007) indicate that the $O(\delta)$ LMRs observed in PIV realizations like that presented in figure 5(*a*) may actually extend several δ in the streamwise direction and meander significantly in the spanwise direction. These 'superstructures' have been found to embody a sizable portion of both the turbulent kinetic energy (TKE) and RSS (Kim & Adrian 1999; Guala *et al.* 2006; Balakumar & Adrian 2007).

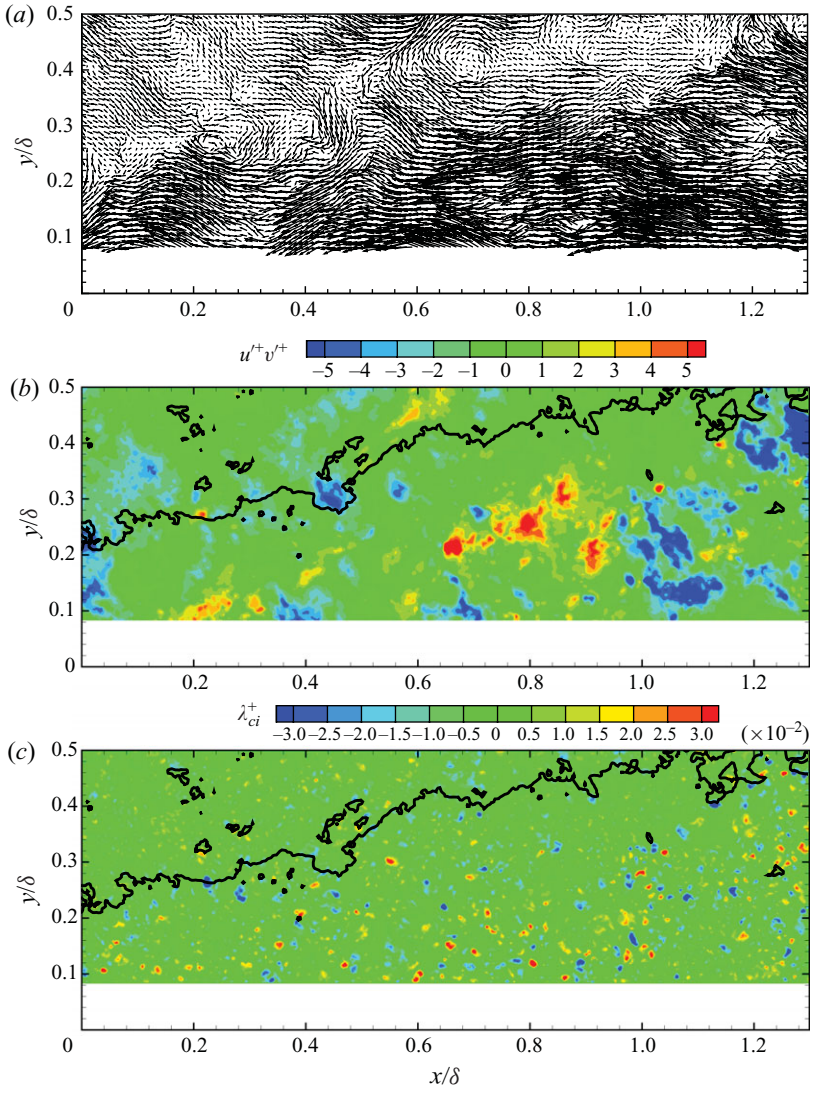

FIGURE 6. A representative instantaneous velocity realization in the streamwise–wall-normal plane of rough-wall flow. (*a*) Galilean decomposition with a constant streamwise advection velocity of $0.74U_e$ removed. (*b*) Instantaneous contributions to RSS, $u'v'$. (*c*) Instantaneous swirling strength, λ_{ci}. Line contours outlining low-momentum interface (with $0.74U_e$ threshold) overlaid in (*b*) and (*c*).

3.2. *Rough-wall flow*

Figure 6(*a*) presents a representative instantaneous velocity field in the x–y plane for flow over the rough surface visualized with a constant advection velocity of $0.74U_e$ removed. The character of this field is quite similar to that in figure 4(*a*) for smooth-wall flow as several prograde spanwise vortices are observed to align roughly in the streamwise direction, forming an inclined interface beneath which a region of significant streamwise momentum deficit exists. The instantaneous inner-scaled $u'v'$ field associated with this velocity field (figure 6*b*) indicates the presence of intense, negative $u'v'$ via ejections of low-speed fluid away from the wall beneath the inclined

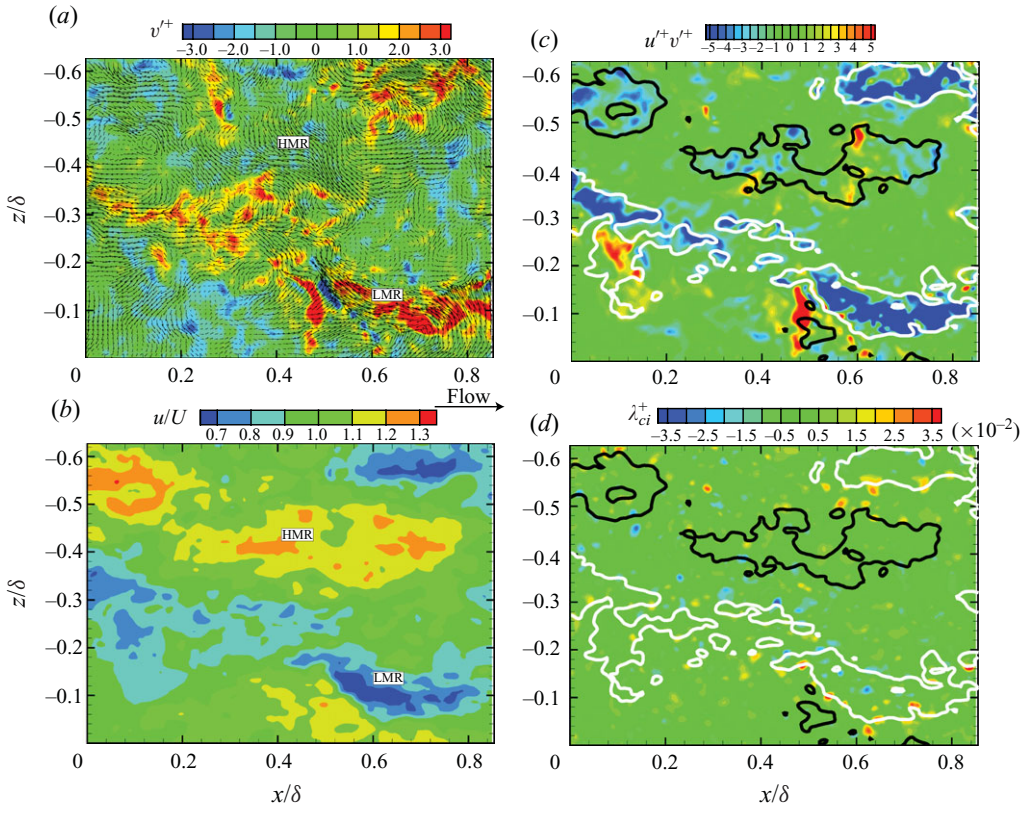

FIGURE 7. A representative instantaneous velocity realization in the streamwise–spanwise plane at $y = 0.15\delta = 4k$ for rough-wall flow. (*a*) Fluctuating in-plane velocities (u', w') are presented as vectors and the fluctuating out-of-plane velocity v' is presented as contours. (*b*) Contours of normalized streamwise velocity, u/U. (*c*) Instantaneous contributions to RSS, $u'v'$. (*d*) Instantaneous swirling strength, λ_{ci}. Line contours of low- (white; $0.85U$) and high-momentum (black; $1.15U$) regions are presented in the background.

interface of the packet (shown as line contours). Further, the instantaneous λ_{ci} field for this velocity realization (figure 6*c*) confirms the alignment of prograde spanwise vortices along the interface of the low-momentum region as well as the presence of several retrograde vortices in close proximity to the prograde cores. All of these characteristics are entirely consistent with those observed in the smooth-wall case, indicating that the overall structural foundation of the outer layer is maintained in the presence of the rough surface considered herein. Volino *et al.* (2007) similarly reported the instantaneous structure of flow over a wire mesh surface to be qualitatively consistent with that of smooth-wall flow.

These consistencies are further supported by the instantaneous character of the rough-wall flow in the x–z plane at $y = 0.15\delta = 4k$. Figure 7(*a*) presents a representative instantaneous velocity realization in this wall-parallel plane for flow over the rough surface. As in the smooth-wall case, an LMR and HMR are readily apparent in this realization, with their spatial extents highlighted in figure 7(*b*). Intense ejections and sweeps of fluid away from and towards the surface, respectively, are notable in figure 7(*c*) which presents instantaneous inner-scaled $u'v'$ for this velocity realization (with line contours demarcating the boundaries of the LMR and HMR)

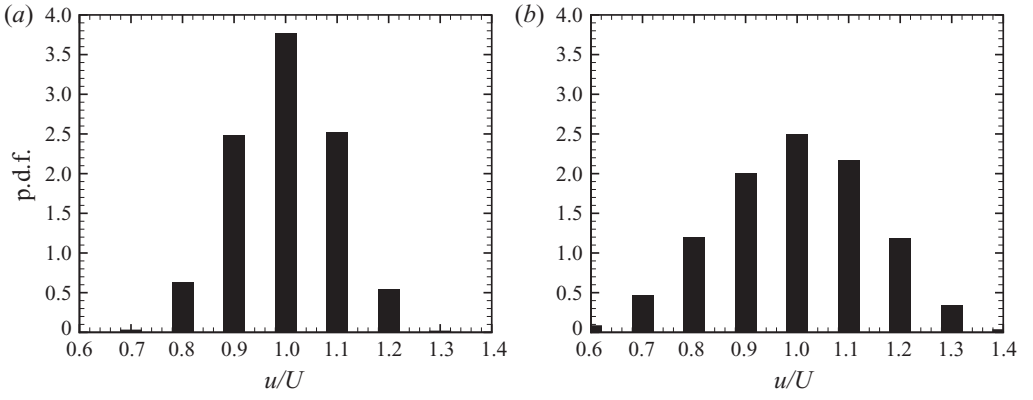

FIGURE 8. P.d.f.s of normalized streamwise velocity, u/U, in the streamwise–spanwise plane at $y = 0.15\delta$ for (a) smooth- and (b) rough-wall flow.

and opposing-sign λ_{ci} events are apparent along the boundaries of the LMR and HMR (figure 7d). These spatial characteristics are again quite consistent in all regards with the smooth-wall field, further supporting the notion that the qualitative aspects of the spatial structure of the turbulence are unaltered by the presence of roughness at this wall-normal location. As such, LMRs and HMRs appear to be robust spatial features of both flows.

Quantitatively, however, some differences between smooth- and rough-wall flow exist. For example, the excursions of the instantaneous streamwise velocity u about the mean U appear to be much stronger in the rough-wall case when figures 5(b) and 7(b) are compared. The extent of these excursions can be quantified by ensemble-averaged p.d.f.s of the normalized instantaneous streamwise velocity, u/U, as presented in figure 8 for the smooth- and rough-wall cases. While the largest excursions of u about the mean are roughly 20 % in the smooth-wall case, these excursions can exceed 40 % in the rough case. In addition, slightly more intense v' fluctuations exist in the rough-wall case which, together with stronger u' fluctuations, lead to slightly more intense $u'v'$ events.

To explore these differences in a more quantitative manner, the contributions of LMRs to various turbulence quantities of interest in the smooth and rough cases are assessed. To facilitate these calculations, a threshold U_{th} on an LMR is established (some fraction of the ensemble- and area-averaged mean streamwise velocity U) and an indicator function, I, is assigned at every grid-point in the jth velocity realization as

$$I(x_j, z_j; U_{th}) = \begin{cases} 1, & \text{when } u(x_j, z_j) \leqslant U_{th}, \\ 0, & \text{otherwise}, \end{cases} \tag{3.1}$$

to distinguish between grid-points that meet the LMR threshold and those that do not. The contributions of the LMRs identified with a given threshold U_{th} to a certain turbulence quantity of interest, $\langle S \rangle$, are then assessed as

$$\langle S \rangle(U_{th}) = \frac{1}{M \times P} \sum_{\text{all } x} \sum_{\text{all } z} \sum_{j=1}^{M} S(x_j, z_j) I(x_j, z_j; U_{th}), \tag{3.2}$$

where M is the total number of velocity realizations and P is the total number of grid-points within a velocity realization (in both the x and z directions). In addition, the

	U_{th}	$\langle u'v' \rangle$	$\langle u'^2 \rangle$	$\langle v'^2 \rangle$	$\langle w'^2 \rangle$	$\langle q^2 \rangle$	Space fraction, N
Smooth	$0.9U$	44 %	40 %	21 %	15 %	31 %	16 %
	$0.8U$	12 %	10 %	4 %	2 %	7 %	2 %
	$0.7U$	0.4 %	0.3 %	0.1 %	0.02 %	0.2 %	0.03 %
Rough	$0.9U$	51 %	48 %	31 %	26 %	39 %	26 %
	$0.8U$	34 %	31 %	13 %	9 %	22 %	9 %
	$0.7U$	12 %	11 %	3 %	2 %	7 %	2 %

TABLE 2. Contributions of LMRs to the Reynolds stresses and TKE for smooth- and rough-wall flow.

fraction of space N occupied by the LMRs satisfying the U_{th} threshold is evaluated as

$$N(U_{th}) = \frac{\sum I(U_{th})}{M \times P}, \tag{3.3}$$

where the summation is over all realizations and grid-points.

Contributions to the RSS, the Reynolds normal stresses ($\langle u'^2 \rangle$, $\langle v'^2 \rangle$ and $\langle w'^2 \rangle$) and the TKE ($\langle q^2 \rangle$) within LMRs for $U_{th} = 0.9U$, $0.8U$ and $0.7U$ are tabulated in table 2. These thresholds were selected because they capture the excursions in streamwise velocity noted in the p.d.f.s of figure 8. For $U_{th} = 0.9U$ (a weak threshold on LMRs since it includes almost all possibilities), the contributions of LMRs to $\langle u'v' \rangle$, $\langle u'^2 \rangle$, $\langle w'^2 \rangle$ and $\langle q^2 \rangle$ are slightly higher in the rough-wall flow compared to the smooth-wall baseline (51 % versus 44 % for $\langle u'v' \rangle$, for example). In addition, the fraction of space occupied by LMRs satisfying $U_{th} = 0.9U$ is 10 % higher in the case of flow over the rough surface. Further, while the space fraction (0.3 %) and associated contributions to the various turbulence statistics (< 0.4 %) for $U_{th} = 0.7U$ are all minimal for smooth-wall flow, they are all at least an order of magnitude larger for the rough case, most notably a space fraction of 2 % and a contribution to $\langle u'v' \rangle$ of 12 %. As such, an increased incidence of LMRs with quite large streamwise momentum deficits is noted in the rough-wall case and these LMRs appear to contribute significantly to the turbulent stresses and kinetic energy.

4. Two-point correlation coefficients

As noted in many recent studies (see e.g. Christensen & Adrian 2001; Tomkins & Adrian 2003; Ganapathisubramani *et al.* 2005), spatial correlations involving two or more points of interest contain a wealth of information regarding the average spatial structure of wall turbulence. Thus, any modifications of the underlying structure of the flow in the presence of roughness can be further explored by directly comparing various spatial correlations for smooth- and rough-wall flow computed from the x–y and x–z PIV data sets. Since the wall-normal direction is statistically inhomogeneous, the two-point velocity correlation coefficients in the x–y plane are given by

$$\rho_{ij}(\Delta x, y; y_{ref}) = \frac{\langle u_i'(x, y_{ref}) u_j'(x + \Delta x, y) \rangle}{\sigma_i(y_{ref}) \sigma_j(y)}, \tag{4.1}$$

where Δx is the spatial separation in the streamwise direction, y_{ref} is the wall-normal reference location and σ_i and σ_j are root-mean-squares of the ith and jth velocity components. In contrast, the velocity correlations computed from the PIV

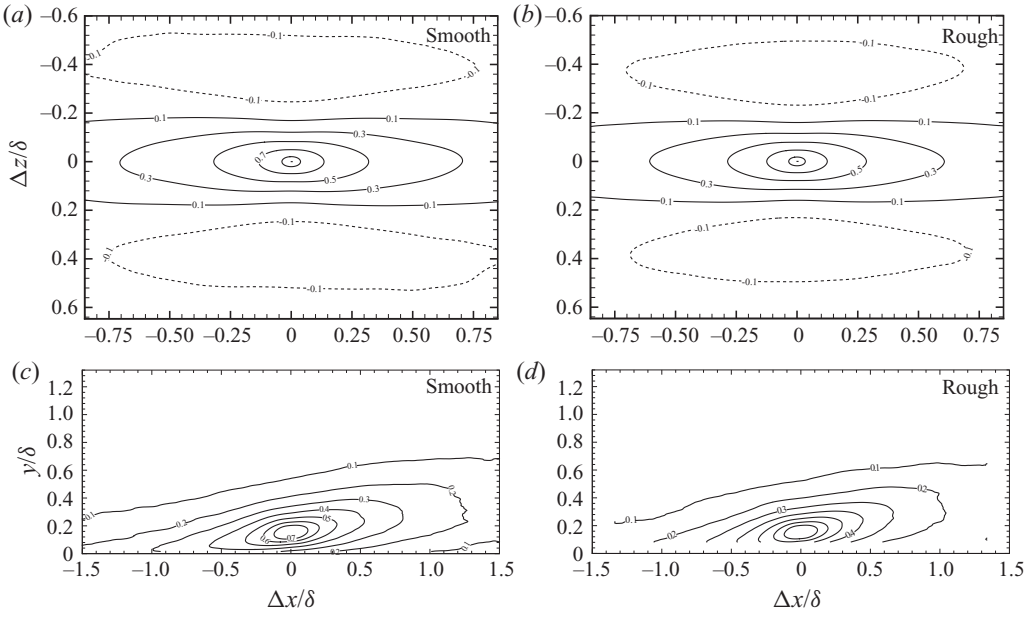

FIGURE 9. Streamwise velocity correlation coefficients ρ_{uu} in the (*a*, *b*) x–z plane ($y = 0.15\delta$) and (*c*, *d*) x–y plane ($y_{ref} = 0.15\delta$) for smooth- and rough-wall flow, respectively.

data acquired in the streamwise–spanwise planes can be expressed as

$$\rho_{ij}(\Delta x, \Delta z; y) = \frac{\langle u_i'(x, y, z) u_j'(x + \Delta x, y, z + \Delta z)\rangle}{\sigma_i(y)\sigma_j(y)}, \tag{4.2}$$

where Δz is the spatial separation in the spanwise direction.

4.1. *Streamwise velocity* (ρ_{uu})

Figures 9(*a*) and 9(*b*) present ρ_{uu} in the x–z plane at $y = 0.15\delta$ for the smooth- and rough-wall flows, respectively. There exists little qualitative difference between ρ_{uu} over the smooth and rough surfaces as they are both elongated in the streamwise direction and are bounded by weak negative, yet streamwise-elongated, correlations in the spanwise direction. These characteristics are quite consistent with previous observations of ρ_{uu} over smooth walls (Tomkins & Adrian 2003; Ganapathisubramani *et al.* 2005) and are likely to be attributable to the aforementioned streamwise-aligned, spanwise-alternating LMRs and HMRs. Figures 9(*c*) and 9(*d*) present contours of ρ_{uu} in the x–y plane at $y_{ref} = 0.15\delta$ for the smooth- and rough-wall flows, respectively. Consistent with the results in the x–z plane at $y = 0.15\delta$, there is again little qualitative difference in ρ_{uu} in the x–y plane for the smooth- and rough-wall cases as it is elongated in the streamwise direction and is slightly inclined away from the wall at its downstream end in both cases. This inclination is similar in magnitude to the inclination noted in instantaneous snapshots of hairpin vortex packets and has therefore been previously interpreted as a structural imprint of such entities (Christensen & Adrian 2001; Christensen & Wu 2005). Taken together with the instantaneous characteristics described earlier, these consistencies in the average character of ρ_{uu} in smooth- and rough-wall flow further indicate that the structural foundation of smooth-wall turbulence near the outer edge of the roughness sublayer is, at least qualitatively, undisturbed by the roughness considered.

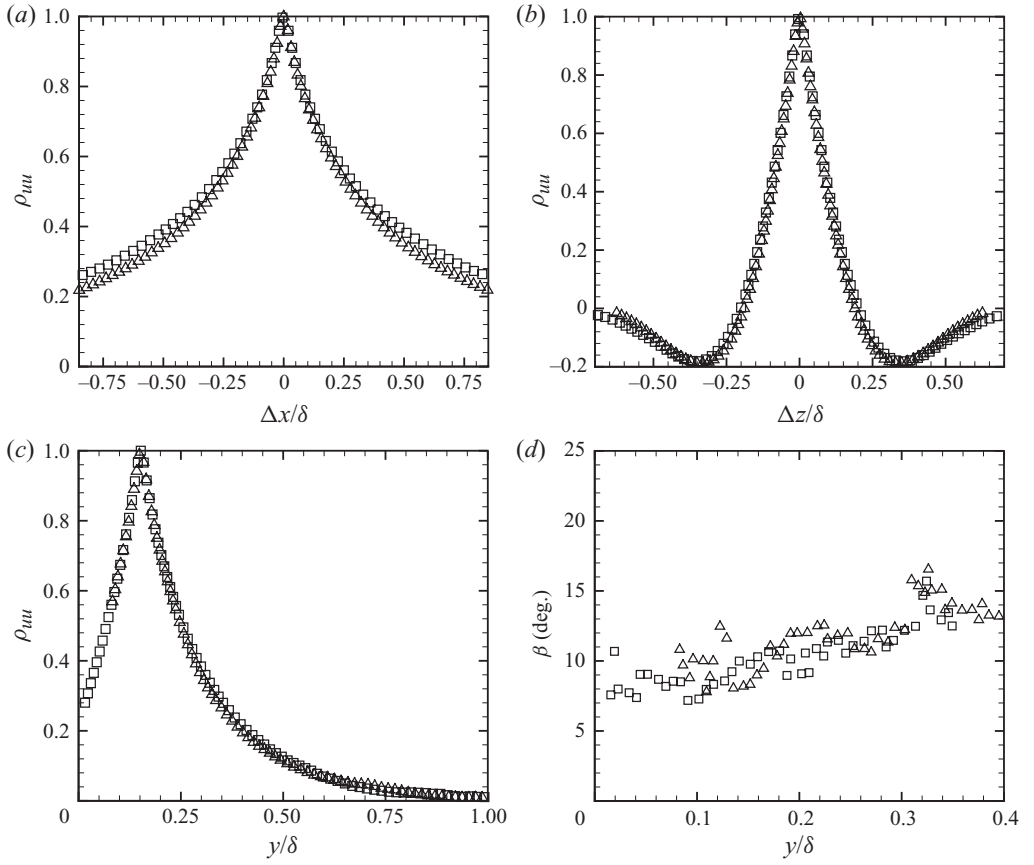

FIGURE 10. One-dimensional profiles of ρ_{uu} from figure 9 in the (a) streamwise, (b) spanwise and (c) wall-normal directions at $y = 0.15\delta$. (d) Average inclination angle of ρ_{uu}, β, as a function of wall-normal position. □: smooth; △: rough.

A more quantitative contrast of ρ_{uu} in the smooth- and rough-wall cases is accomplished by comparing one-dimensional profiles of ρ_{uu} in all three spatial directions for $y_{ref} = 0.15\delta$ as presented in figure 10 (note that symbol size accommodates the uncertainty in the correlation coefficients throughout). While consistency is observed in the spanwise (figure 10b) and wall-normal (figure 10c) directions, a noted shortening of ρ_{uu} in the streamwise direction is apparent in the presence of roughness (figure 10a). For example, at a correlation level of 0.3, the streamwise extent of ρ_{uu} is approximately 18 % shorter in the rough-wall case than the smooth-wall baseline. Similar comparisons for $y < 0.15\delta$ using x–y data show enhanced shortening as the surface is approached, while comparisons for $y > 0.15\delta$ indicate a weakening of this shortening, though differences between the smooth- and rough-wall cases still exist well outside the roughness sublayer (neither shown for brevity; see Wu & Christensen 2007 and Wu 2008). Given that the elongated streamwise extent of ρ_{uu} is likely to be tied to that of large-scale vortex organization, this reduction indicates some level of quantitative impact of roughness on this important structural feature of wall turbulence. Of interest, this observation is similar to the results of both Krogstad & Antonia (1994) and Volino *et al.* (2007) for turbulent flow over mesh roughness. Further, Tomkins (2001) observed a noted shortening in

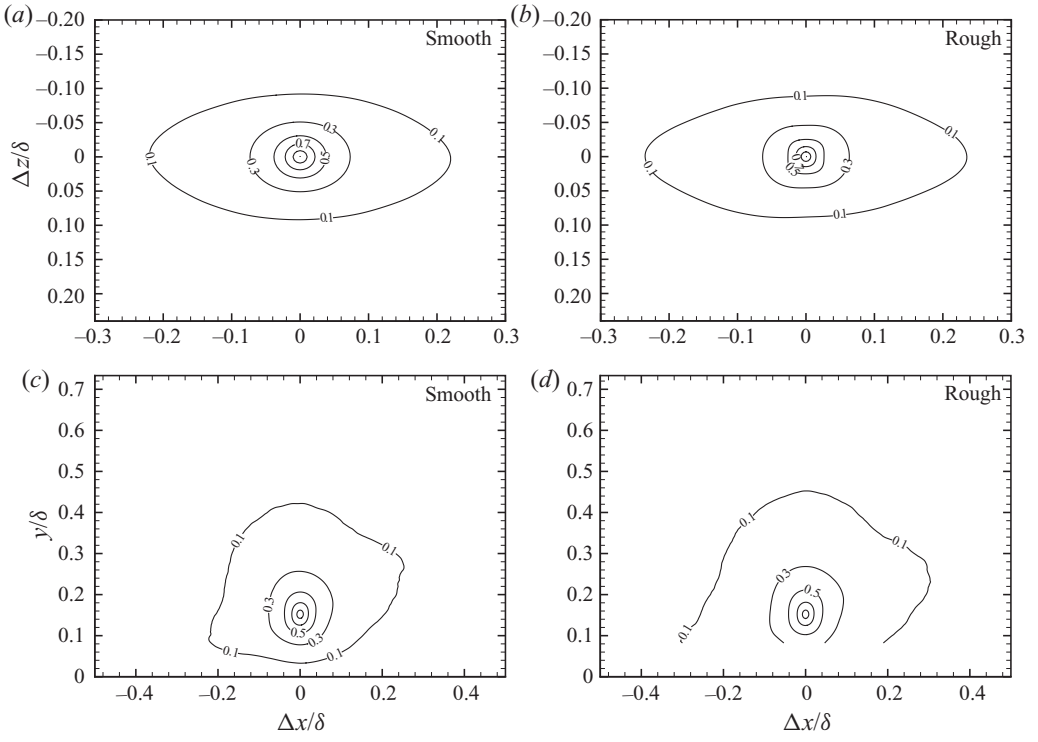

FIGURE 11. Wall-normal velocity correlation coefficients ρ_{vv} in the (*a*, *b*) x–z plane ($y = 0.15\delta$) and (*c*, *d*) x–y plane ($y_{ref} = 0.15\delta$) for smooth- and rough-wall flow, respectively.

ρ_{uu} immediately downstream of small ($k \ll \delta$) hemispheres sparsely distributed in a turbulent boundary layer. Thus, the present observations for irregular roughness are in line with similar observations for flow over more idealized roughness.

With respect to the inclination angle of ρ_{uu} in the x–y plane, a quantitative comparison of this angle, β, can be accomplished by fitting a line through the point at each contour level that exists farthest away from the reference location (Christensen & Wu 2005). Figure 10(*d*) presents β as a function of wall-normal position for both flows and little sensitivity to the rough wall is observed both above and below the $y = 0.15\delta$ wall-normal position considered herein. While some scatter in the data exists, both the smooth- and rough-wall inclination angles increase slightly with wall-normal position, consistent with past observations in smooth-wall turbulence (Christensen & Wu 2005). This agreement is also consistent with the observations of Volino *et al.* (2007) for flow over wire mesh but counter to the marked increase in inclination angle reported by Krogstad & Antonia (1994) for flow over wire mesh.

4.2. *Wall-normal velocity* (ρ_{vv})

Figure 11 presents contours of ρ_{vv} in the x–z plane at $y = 0.15\delta$ and in the x–y plane at $y_{ref} = 0.15\delta$ for both smooth- and rough-wall flows. As has been reported previously for smooth-wall flows, ρ_{vv} is far less elongated in the streamwise and spanwise directions compared to ρ_{uu} and its spatial signature near the origin is interpreted as the imprint of the individual hairpin-like vortices in a packet (Christensen & Wu 2005). Contrasting the smooth- and rough-wall results, ρ_{vv} appears insensitive to roughness at this wall-normal location. A more quantitative comparison of ρ_{vv}

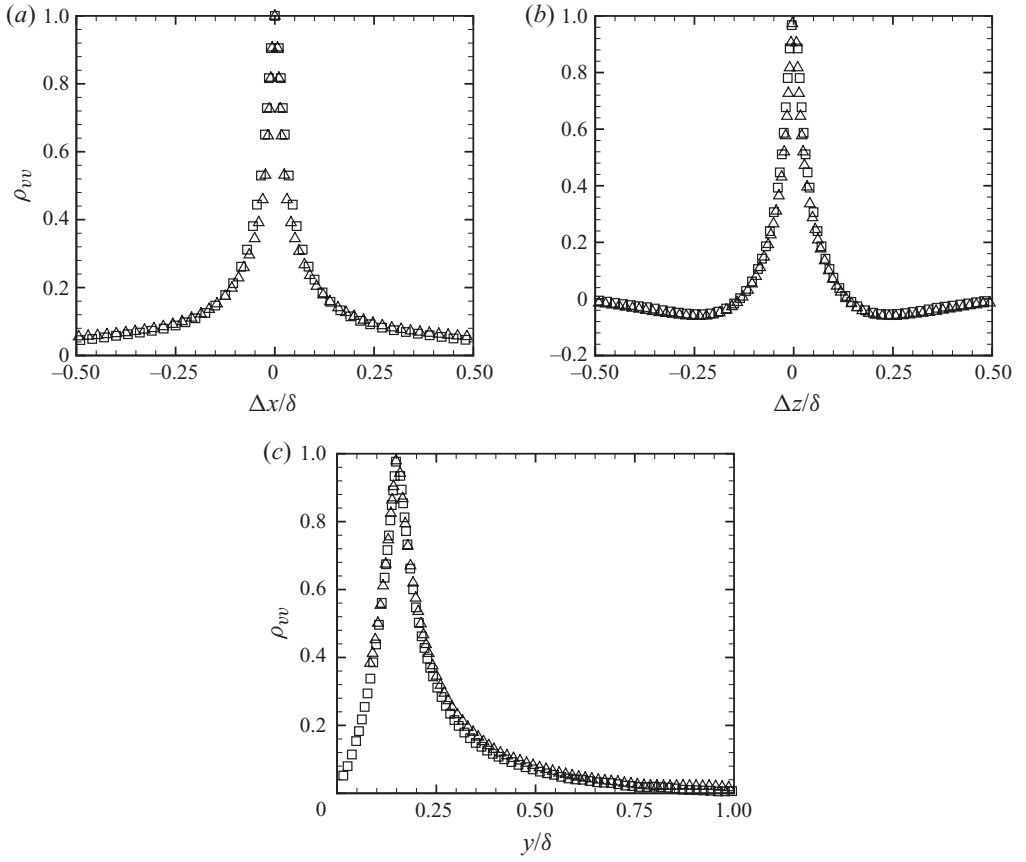

FIGURE 12. One-dimensional profiles of ρ_{vv} from figure 11 in the (a) streamwise, (b) spanwise and (c) wall-normal directions at $y = 0.15\delta$. □: smooth; △: rough.

is presented in figure 12 where one-dimensional profiles of ρ_{vv} in the streamwise, spanwise and wall-normal directions are shown. Collapse of the smooth- and rough-wall profiles is noted in all three spatial directions, indicating a strong similarity in the smaller spatial scales of these flows.

4.3. *Spanwise velocity* (ρ_{ww})

Figures 13(a) and 13(b) present ρ_{ww} in the x–z plane at $y = 0.15\delta$ for smooth- and rough-wall flows (ρ_{ww} is not shown in the x–y plane since w was not resolved in the two-dimensional PIV measurements). The spatial extent of ρ_{ww} is slightly larger than that of ρ_{vv} but significantly smaller than that of ρ_{uu} and these results indicate that the spanwise and streamwise extents of ρ_{ww} are relatively insensitive to roughness effects. This consistency is evident in figures 13(c) and 13(d) which present one-dimensional slices of ρ_{ww} in the streamwise and spanwise directions, respectively. For reference, these rough-wall ρ_{ww} trends are similar to those reported by Volino *et al.* (2007) but counter to the decrease in the streamwise extent of ρ_{ww} reported by Krogstad & Antonia (1994) for flow over wire mesh.

4.4. *Wall-normal vortex cores* ($\rho_{\lambda_y\lambda_y}$)

As noted earlier, swirling strength is an effective tool for identifying vortices in the x–y and x–z instantaneous velocity fields. In the case of the measurements in

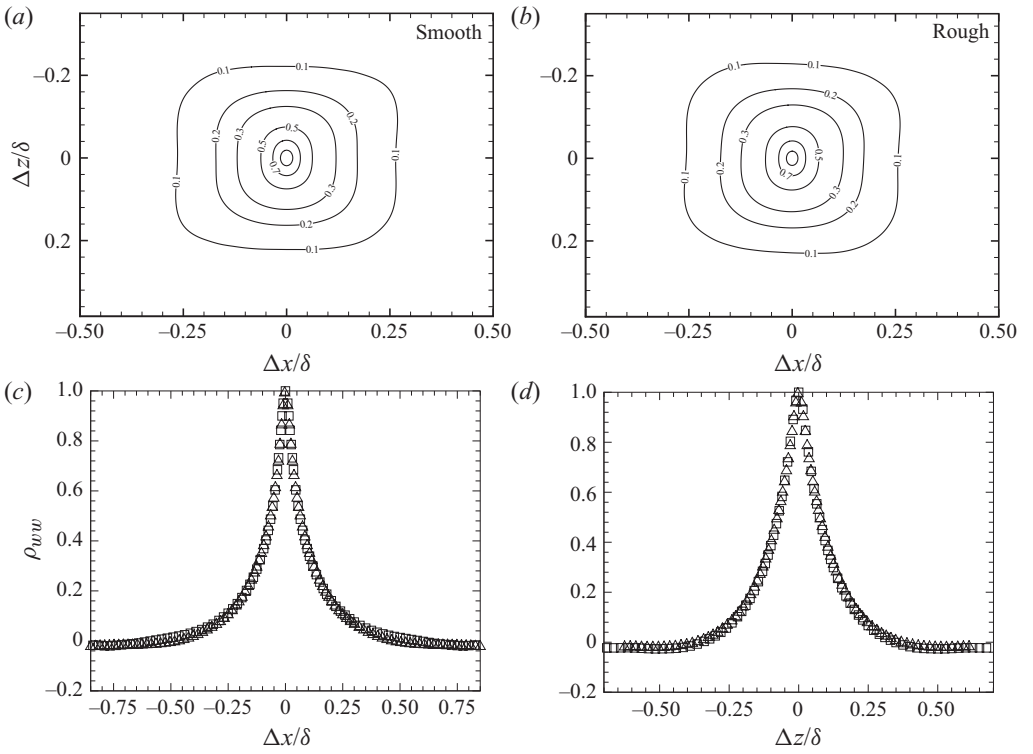

FIGURE 13. (*a*, *b*) Spanwise velocity correlation coefficients, ρ_{ww}, in the x–z plane at $y = 0.15\delta$ for smooth- and rough-wall flow, respectively. (*c*, *d*) One-dimensional profiles of ρ_{ww} in the streamwise and spanwise directions, respectively. □: smooth; △: rough.

the x–z plane at $y = 0.15\delta$, the identified vortices are wall-normal in orientation and, given their clustering outboard of LMRs (figures 5 and 7), are interpreted as slices through the arched legs/necks of hairpin-like structures. In this context, wall-normal vortices with the same rotational sense would be expected to align approximately in the streamwise direction due to the streamwise alignment of vortices in hairpin packets. To assess the average spatial characteristics of these structures, two-point correlations of wall-normal swirling strength (λ_y), $\rho_{\lambda_y\lambda_y}$, are presented in figures 14(*a*) and 14(*b*) for smooth- and rough-wall flow at $y = 0.15\delta$. These correlations display two distinct spatial characteristics: compact, roughly circular contours centred at $(\Delta x, \Delta z) = (0, 0)$ and weaker contour levels elongated in the streamwise direction. The compact contours can be interpreted as the imprint of the individual wall-normal vortex cores that populate the x–z plane at $y = 0.15\delta$. In contrast, the streamwise-elongated contours are more consistent with correlation between consecutive, streamwise-aligned hairpin-like structures in vortex packets as first noted by Tomkins & Adrian (2003). Interestingly, both the streamwise and spanwise extents of $\rho_{\lambda_y\lambda_y}$ are reduced in the presence of roughness, most notably the weaker, streamwise-elongated correlation levels. This reduction in overall streamwise coherence is similar to that noted in ρ_{uu}, further indicating that the streamwise characteristics of outer-layer vortex organization are affected by surface roughness.

To assess these differences in a more quantitative manner, figures 14(*c*) and 14(*d*) present one-dimensional profiles of $\rho_{\lambda_y\lambda_y}$ in the streamwise and spanwise directions at $y = 0.15\delta$ scaled in outer units. As was noted in the two-dimensional contours in

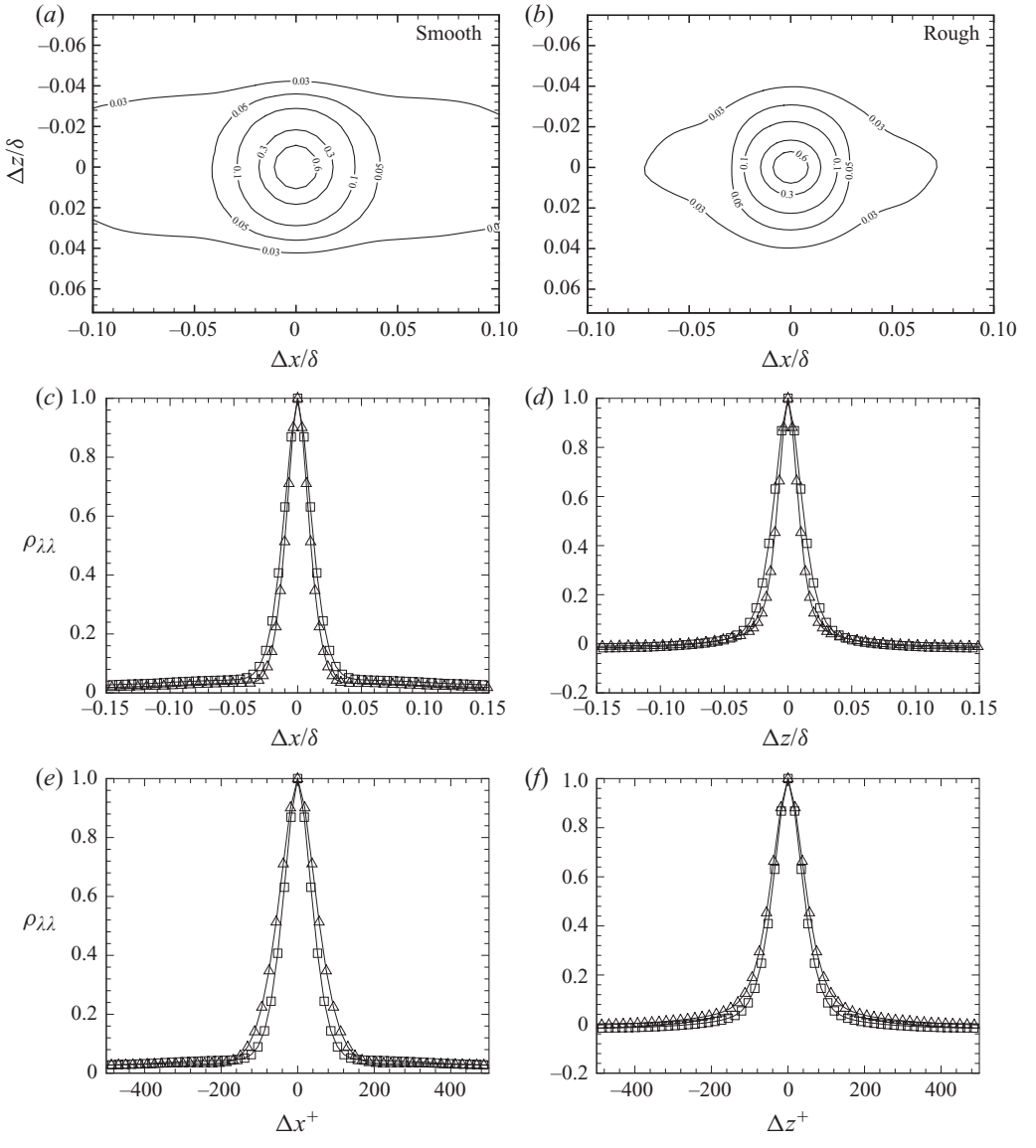

FIGURE 14. (*a*, *b*) Wall-normal swirling strength correlation coefficients, $\rho_{\lambda_y\lambda_y}$, in the x–z plane at $y = 0.15\delta$ for smooth- and rough-wall flow, respectively. (*c*, *d*) Outer- and (*e*, *f*) inner-scaled, one-dimensional profiles of $\rho_{\lambda_y\lambda_y}$ in the streamwise and spanwise directions, respectively. □: smooth; △: rough.

figures 14(*a*) and 14(*b*), scaling in outer units highlights the reduction in the streamwise and spanwise extents of $\rho_{\lambda_y\lambda_y}$ in the presence of roughness. However, when these one-dimensional profiles are instead plotted on spatial separations normalized in inner units (figures 14*e* and 14*f*), a slightly better collapse is noted for smaller spatial separations in both directions. This inner-scale collapse of $\rho_{\lambda_y\lambda_y}$ is in accordance with recent experimental evidence suggesting that the diameters of small-scale vortex cores in smooth-wall turbulence scale more appropriately on viscous scales, such as y_* or η (the Kolmogorov length scale) (Carlier & Stanislas 2005; Wu & Christensen 2006; Stanislas, Perret & Foucat 2008).

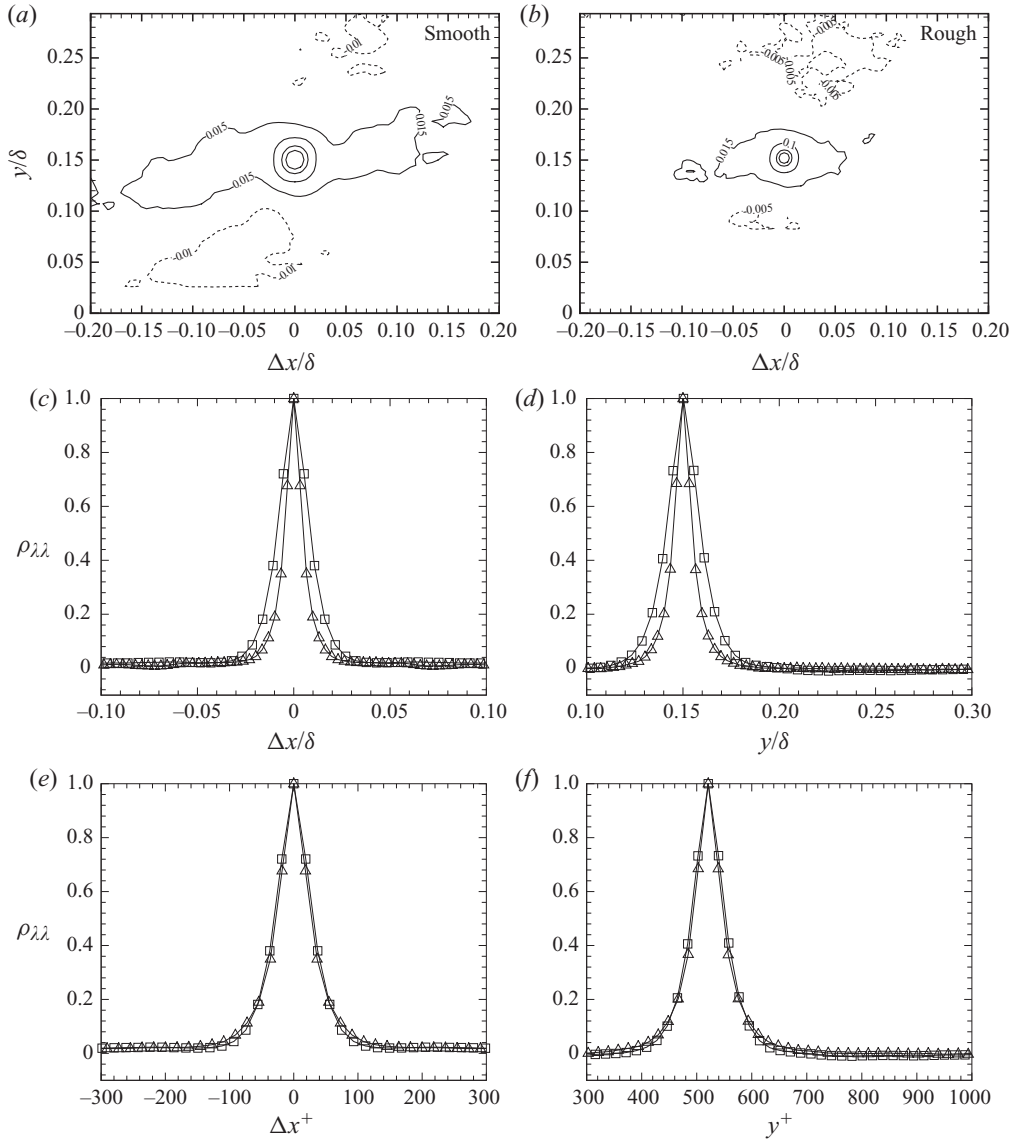

FIGURE 15. (*a*, *b*) Spanwise swirling strength correlation coefficients, $\rho_{\lambda_z\lambda_z}$, in the x–y plane at $y_{ref} = 0.15\delta$ for smooth- and rough-wall flow, respectively. (*c*, *d*) Outer- and (*e*, *f*) inner-scaled, one-dimensional profiles of $\rho_{\lambda_z\lambda_z}$ in the streamwise and wall-normal directions, respectively. □: smooth; △: rough.

4.5. *Spanwise vortex cores* ($\rho_{\lambda_z\lambda_z}$)

Figure 15 presents two-point correlations of spanwise swirling strength (λ_z), $\rho_{\lambda_z\lambda_z}$, in the x–y plane at $y_{ref} = 0.15\delta$ for flow over the smooth and rough surfaces. Both smooth- and rough-wall $\rho_{\lambda_z\lambda_z}$ are characterized by compact circular contours, likely to be the imprint of individual spanwise vortices, as well as weaker streamwise-elongated contours that are inclined slightly away from the wall. These latter characteristics probably reflect the spatial correlation of the heads of consecutive streamwise-aligned hairpin structures in a given vortex packet. In this regard, the inclination of $\rho_{\lambda_z\lambda_z}$ is approximately 10° for both the smooth and rough cases which is similar to

the inclination angles of ρ_{uu} in the x–y plane (figure 10d). Despite these qualitative consistencies, the streamwise coherence of $\rho_{\lambda_z\lambda_z}$ is reduced considerably in the presence of roughness as was noted for both ρ_{uu} and $\rho_{\lambda_y\lambda_y}$.

The smooth- and rough-wall $\rho_{\lambda_z\lambda_z}$ also both contain weak negative correlation levels downstream of and above as well as upstream of and below the central correlation peak at $(\Delta x, y) = (0, y_{ref} = 0.15\delta)$. These negative correlation values reflect the occurrence of spatially coincident prograde and retrograde spanwise vortices. Natrajan *et al.* (2007) first reported these regions of negative correlation in $\rho_{\lambda_z\lambda_z}$ and postulated the latter arrangement to be a slice through the shoulder of an omega-shaped hairpin-like structure while the former arrangement may be due to ring-like vortices that have been previously reported in smooth-wall turbulence (e.g. Falco 1991). Interestingly, these regions of negative correlation in $\rho_{\lambda_z\lambda_z}$ become smaller and weaker in the rough-wall flow. Finally, one-dimensional profiles of $\rho_{\lambda_z\lambda_z}$ in the streamwise and wall-normal directions are shown in figures 15(c) and 15(d) in outer units and figures 15(e) and 15(f) in inner units. Good collapse on y_* is observed, consistent with the trends noted for $\rho_{\lambda_y\lambda_y}$, indicating again that the diameters of these vortex cores scale on viscous scales.

5. Proper orthogonal decomposition analysis

Based on the correlations presented in § 4, it seems that the present roughness has little impact on the smaller scales of the flow while modifying the streamwise coherence of the larger scales. To explore these similarities and differences further, POD is employed to define suitable sets of basis functions for the present velocity ensembles which are then used to effectively separate larger- and smaller-scale features of the flow. Snapshot POD is used as it is more amenable to the discrete nature of PIV velocity fields and data sets than the classical POD formulation (Sirovich 1987).

Following Cazemier, Verstappen & Veldman (1998), the goal of snapshot POD analysis is to determine the best approximation of a given instantaneous turbulent velocity field, $u(x, t)$, in terms of N deterministic spatial POD modes $\phi_i(x)$, $i = 1, \ldots, N$ and N random temporal functions $a_i(t)$, $i = 1, \ldots, N$. Mathematically, this problem can be expressed as

$$\min \int_\Omega \int_T \left\{ u(x,t) - \sum_{i=1}^{N} a_i(t)\phi_i(x) \right\}^2 \mathrm{d}t\, \mathrm{d}x, \tag{5.1}$$

where the integrations are over the spatial domain Ω and a time interval T. Arbitrary variations of the unknowns $\phi_i(x)$ and $a_i(t)$ lead to

$$\int_T \left(u - \sum_j a_j\phi_j \right) a_i \,\mathrm{d}t = 0 = \int_\Omega \left(u - \sum_j a_j\phi_j \right) \phi_i \,\mathrm{d}x. \tag{5.2}$$

Assuming orthogonality of $\phi(x)$ and $a(t)$ in POD analysis ($\int_\Omega \phi_i\phi_j \,\mathrm{d}x = 0 = \int_T a_i a_j \,\mathrm{d}t$ for $i \neq j$), (5.2) can be simplified as

$$\phi_i(x) = \frac{\displaystyle\int_T u a_i \,\mathrm{d}t}{\displaystyle\int_T a_i^2 \,\mathrm{d}t} \tag{5.3}$$

and

$$a_i(t) = \frac{\int_\Omega u\phi_i \, \mathrm{d}x}{\int_\Omega \phi_i^2 \, \mathrm{d}x}. \tag{5.4}$$

Substituting (5.4) into (5.3) yields the eigenvalue problem with a positive definite Hermitian kernel of the form

$$\lambda_i a_i(t) = \int_T \left(\int_\Omega u(x,t)u(x,t') \, \mathrm{d}x \right) a_i(t') \, \mathrm{d}t'. \tag{5.5}$$

Equation (5.5) shows that the temporal coefficients, $a_i(t)$, are the eigenfunctions of the integral operator with the spatial auto-correlation of $u(x,t)$ as a kernel. In addition, the eigenvalues λ_i are real and positive and form a decreasing and convergent series.

POD analysis is typically performed on the fluctuating velocity fields, meaning that the ith eigenvalue λ_i represents the turbulent kinetic energy contribution of the ith POD mode ϕ_i and the fractional contribution of the ith POD mode to the total TKE E_i can be expressed as

$$E_i = \frac{\lambda_i}{E}, \tag{5.6}$$

where $E = \sum_{i=1}^{N} \lambda_i$ is twice the total turbulent kinetic energy of the flow. Further, it can be shown that POD eigenfunctions are optimal in the sense that, for a given number of modes K ($< N$), the projection on the subspace spanned by the K leading POD eigenfunctions contains the largest TKE on average compared to any other set of basis functions. In addition, a low-order reconstruction of any given instantaneous fluctuating field at t_n using the leading K POD modes can be realized as

$$u_L(x,t_n) = \sum_{k=1}^{K} a_k(t_n)\phi_k(x), \tag{5.7}$$

which necessarily generates a residual field, composed of the motions within the discarded higher-order modes, of the form

$$u_R(x,t_n) = \sum_{k=K+1}^{N} a_k(t_n)\phi_k(x) = u(x,t_n) - u_L(x,t_n). \tag{5.8}$$

The use of snapshot POD to analyse PIV ensembles is well-established as many recent studies have employed this method to study the character of the most energetic flow scales (Geers, Tummers & Hanjalic 2005; Kostas, Soria & Chong 2005, among others). In the present effort, snapshot POD is employed to study the characteristics of the larger and smaller scales of the flow over the smooth and rough surfaces using both the x–y and x–z data sets.

5.1. *Streamwise–wall-normal plane*

Snapshot POD analysis is first performed on the streamwise and wall-normal fluctuating velocity components (u', v') from the two-dimensional PIV ensembles in the x–y plane. This analysis is carried out over the wall-normal domain $y \leqslant 0.5\delta$ using 2000 instantaneous velocity fields (snapshots) per flow condition. Only 50 % of the boundary-layer thickness was selected for analysis in order to reduce the computational cost of this analysis and because the behaviour in the vicinity of the surface is the focus of the present contribution. It should be noted that the

Mode n	1	2	3	4	5	6	7	8	9	10
Smooth	0.235	0.092	0.057	0.045	0.029	0.024	0.018	0.018	0.014	0.014
Rough	0.245	0.097	0.058	0.045	0.033	0.024	0.019	0.018	0.014	0.013

TABLE 3. Fractional energy contributions of the first 10 POD modes in the x–y plane.

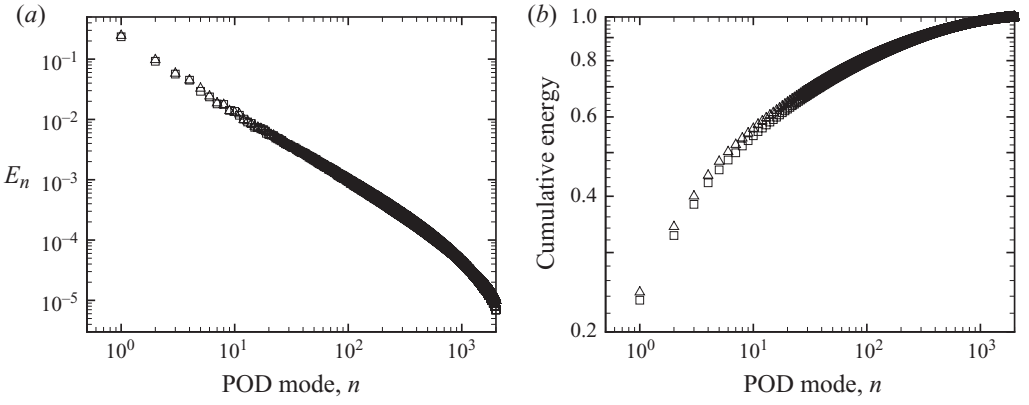

FIGURE 16. POD energy distributions in the x–y plane. (a) Fractional contribution of each POD mode to the total energy, E_n; (b) Cumulative energy distribution. □: smooth; △: rough.

present two-dimensional PIV ensembles only allow the calculation of the u'^2 and v'^2 contributions to the total TKE. However, this resolved TKE ($\langle u'^2 + v'^2 \rangle$) has been shown to effectively capture the general trends of wall turbulence when compared to previously reported DNS studies that provide a full representation of the TKE (e.g. Liu *et* al. 2001).

Figure 16(a) presents the fractional contributions of individual POD modes to the total turbulent kinetic energy E_i for flow over the smooth and rough surfaces. Lower-order POD modes are representative of larger-scale energy-containing features of the flow while higher-order POD modes correspond to smaller-scale and less energetic turbulent events (Holmes, Lumley & Berkooz 1996). The smooth- and rough-wall energy distributions are quite similar throughout the range of POD modes. The fractional energy contributions of the first 10 POD modes for flow over the smooth and rough surfaces are tabulated in table 3. The fractional energy content of the first two POD modes, which embody the largest scales of the flow, are slightly higher (∼4 %) in the presence of roughness. However, these differences diminish quickly with increasing mode number. Figure 16(b) presents the distribution of cumulative energy defined as

$$\text{cumulative energy contained in modes 1 to } m = \sum_{1}^{m} E_i, \tag{5.9}$$

computed from the energy spectra in figure 16(a). The smooth- and rough-wall cumulative POD energy profiles collapse well except for the first two modes. Of interest, more than 400 modes are needed to capture 95 % of the resolved TKE ($\langle u'^2 + v'^2 \rangle$) from the x–y plane PIV measurements in both flows. Thus, the present flows are quite complex owing to the wide range of dynamically important spatial scales present at $Re_\theta \approx 13\,000$.

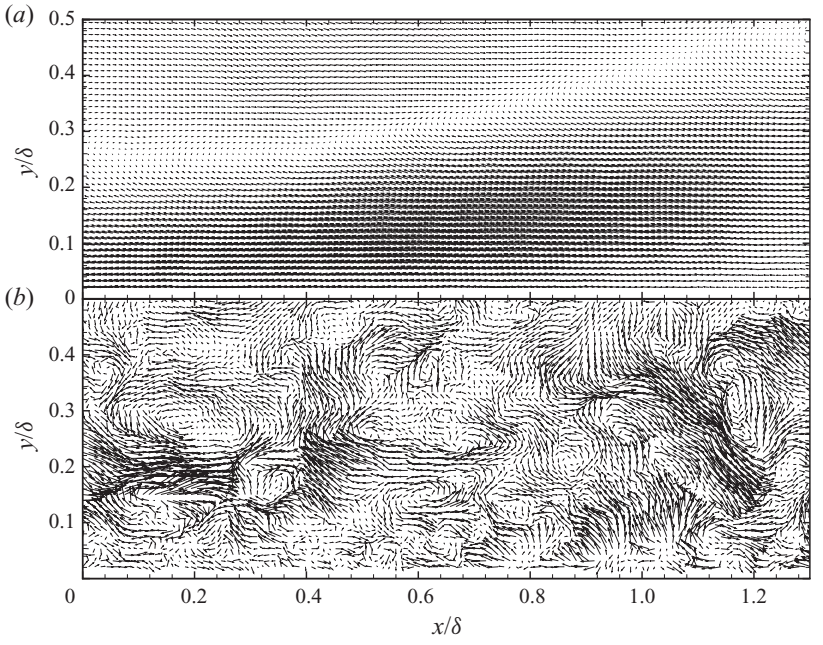

FIGURE 17. (*a*) Low-order (large-scale) representation of the smooth-wall instantaneous velocity realization in figure 4 (projected onto the first five POD modes). (*b*) Associated residual (small-scale) velocity field. Not every vector is shown for clarity.

One of the most beneficial uses of the POD basis functions is to low- and high-pass filter instantaneous velocity realizations in order to study the physics of the larger and smaller scales of each flow. Such a decomposition enables one to separately assess any roughness-induced modifications of the larger and smaller spatial scales. Low-order, or large-scale, velocity fields are generated by reconstructing each individual fluctuating velocity field (or snapshot) using (5.7) from a subset of the leading (most energetic) POD modes. In the present analysis, the number of modes employed in this reconstruction is chosen to be the minimum number required to capture 50 % of the resolved TKE in the two-dimensional x–y plane measurements ($\langle u'^2 + v'^2 \rangle$). As such, the leading six POD modes are used for smooth-wall flow while the first five modes are used for the rough-wall flow. The resulting reconstructed velocity fields represent low-order (larger-scale) representations of the original fluctuating velocity fields while the difference between a given original fluctuating velocity field and its associated low-order field yields a residual (smaller-scale) field given by (5.8). Thus, the ensemble of residual velocity fields for a given flow condition contains the remaining 50 % of the resolved TKE.

Figure 17(*a*) presents the low-order (large-scale) velocity field associated with the smooth-wall instantaneous realization in the x–y plane presented in figure 4. This low-order reconstruction captures the inclined interface and the associated large-scale region of streamwise momentum deficit of the original field but the smaller-scale vortices that line the inclined interface in the original field are not evident in this reconstruction. As such, this low-order field only reflects the gross features of the hairpin vortex packet observed in the original instantaneous field. In contrast, the associated residual velocity field (figure 17*b*) embodies the smaller-scale swirling motions of the hairpin heads as well as the intermittent, yet intense, ejections and

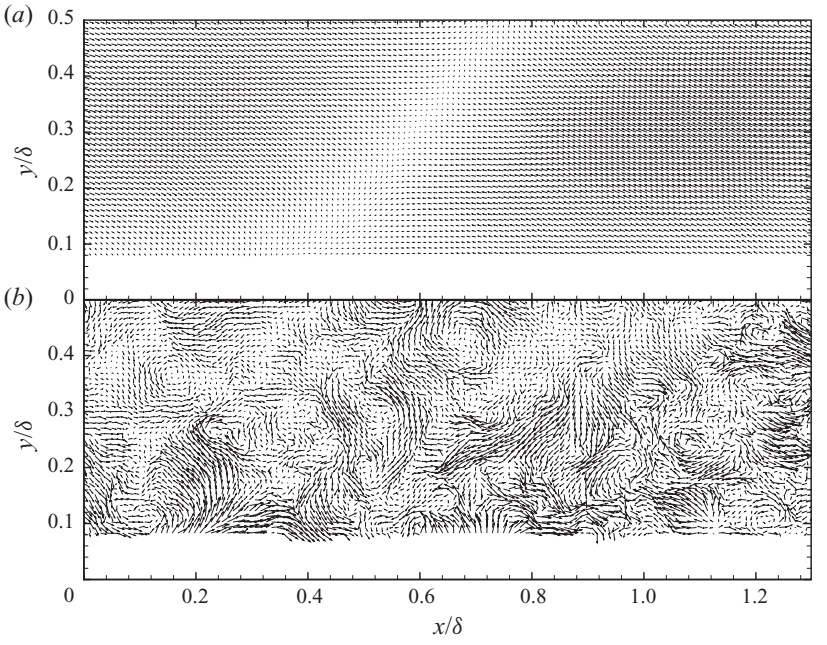

FIGURE 18. (*a*) Low-order (large-scale) representation of the rough-wall instantaneous velocity realization in figure 6 (projected onto the first six POD modes). (*b*) Associated residual (small-scale) velocity field. Not every vector is shown for clarity.

sweeps generated by these structures. Likewise, figure 18(*a*) presents the large-scale velocity field associated with the rough-wall instantaneous realization presented in figure 6 and it again captures only the gross, large-scale structural features of the original field. In contrast, the associated residual field (figure 18*b*) captures the smaller-scale spanwise vortices of the original field as well as the intermittent RSS-producing events.

While visualization of the instantaneous low-order and residual velocity fields provides a glimpse of the large- and small-scale features of these flows, it does not provide quantitative measures of the influence of roughness on these spatial scales. Instead, one can compute contributions of the larger and smaller scales to the Reynolds normal and shear stresses by ensemble- and line-averaging the low-order and residual ensembles separately for each flow condition. This process generates profiles of Reynolds normal and shear stresses attributable to the larger and smaller spatial scales, respectively, and comparison of these profiles to the total profiles provides a measure of the importance of these spatial scales to the overall turbulent stresses in both flows.

Figure 19(*a*) presents profiles of $\langle u'^2\rangle^+$ computed from the original fluctuating velocity fields (referred to as the 'total' profiles) as well as from the low-order and residual ensembles for smooth- and rough-wall flow. As reported by Wu & Christensen (2007), the total profiles of $\langle u'^2\rangle^+$ display similarity in the outer region in accordance with Townsend's wall similarity hypothesis. Interestingly, the low-order and residual contributions to $\langle u'^2\rangle^+$ also display this similarity as the smooth- and rough-wall results collapse reasonably well outside the roughness sublayer ($y \gtrsim 0.2\delta$). In addition, the larger-scale features of the flow generate the vast majority of $\langle u'^2\rangle^+$ everywhere except near $y = 0.1\delta$. In contrast, the smaller scales of the flow dominate

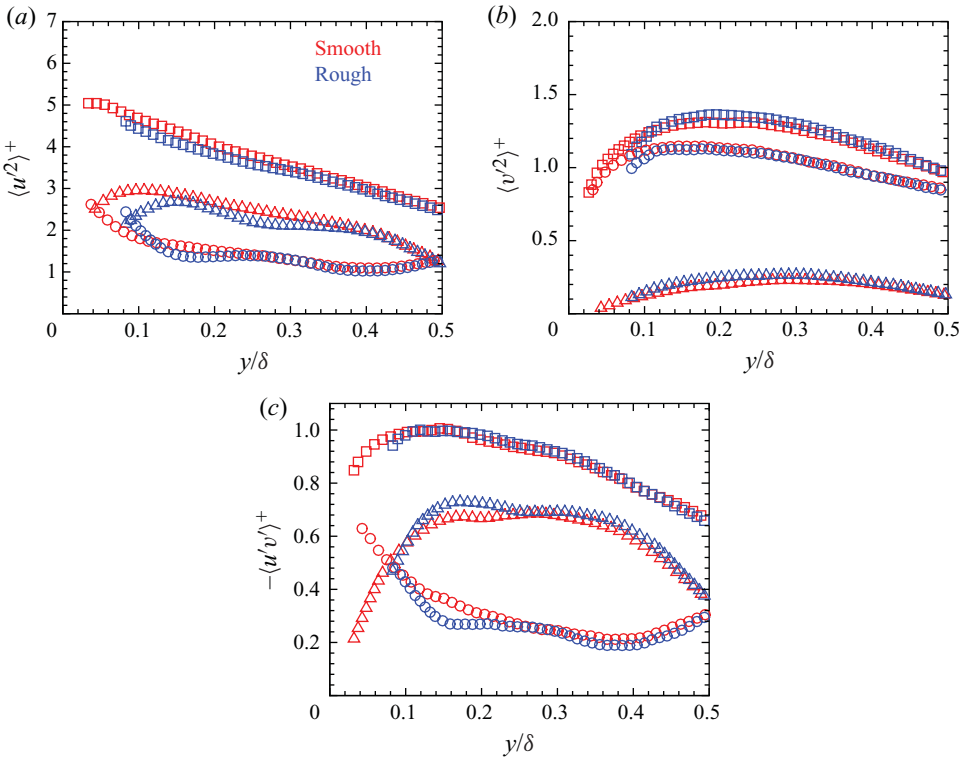

FIGURE 19. Comparison of Reynolds stress contributions from low-order and residual velocity fields for smooth- and rough-wall flow. (*a*) $\langle u'^2\rangle$; (*b*) $\langle v'^2\rangle$; (*c*) $-\langle u'v'\rangle$. □: total statistic; △: low-order contribution; ○: residual contribution. Not every data point is shown for clarity.

$\langle v'^2\rangle^+$ (figure 19*b*) in both the smooth- and rough-wall cases with only a small fraction of $\langle v'^2\rangle^+$ carried by the larger spatial scales of both flows. As with $\langle u'^2\rangle^+$, the contributions to $\langle v'^2\rangle^+$ from large and small scales collapse in the outer layer. Finally, the contributions of larger and smaller scales to $\langle u'v'\rangle^+$ along with the total profiles of $\langle u'v'\rangle^+$ are presented in figure 19(*c*). For $y > 0.1\delta$, the larger spatial scales embody a significant fraction of $\langle u'v'\rangle^+$ – roughly twice that contained in the smaller scales. This trend is consistent with the larger-scale contributions to $\langle u'^2\rangle^+$ in the outer layer. As with the Reynolds normal stresses, the larger- and smaller-scale contributions to $\langle u'v'\rangle^+$ collapse outside the roughness sublayer irrespective of surface condition.

5.2. *Streamwise–spanwise plane*

Snapshot POD is also applied to the smooth- and rough-wall PIV ensembles in the x–z plane at $y = 0.15\delta$ using 1600 snapshots per flow condition. Since these ensembles were acquired using stereo PIV, POD is applied to all three velocity components in this wall-parallel plane. The POD energy distributions for smooth- and rough-wall flow are presented in figure 20. The fractional energy contributions (figure 20*a*) as well as the cumulative POD energy distributions (figure 20*b*) are quite similar between the two flows. This consistency is seen in a quantitative sense in table 4 which lists the fractional energy contributed by the 10 most energetic POD modes for both flows. As was done with the velocity ensembles in the x–y plane, the POD basis functions in this x–z plane are used to generate ensembles of low-order and residual velocity

Mode n	1	2	3	4	5	6	7	8	9	10
Smooth	0.124	0.095	0.061	0.035	0.033	0.030	0.019	0.018	0.016	0.015
Rough	0.124	0.093	0.057	0.035	0.031	0.021	0.019	0.018	0.018	0.016

TABLE 4. Fractional energy contributions of the first 10 POD modes in the x–z plane at $y = 0.15\delta$.

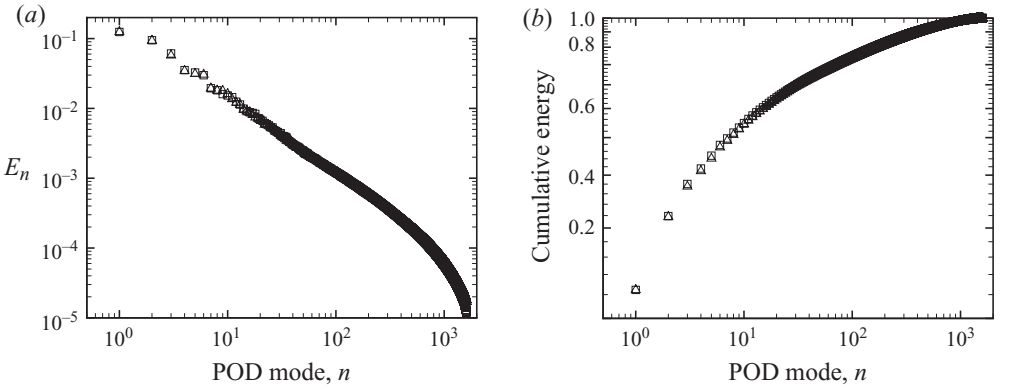

FIGURE 20. POD energy distributions in the x–z plane at $y = 0.15\delta$. (a) Fractional contribution of each POD mode to the total energy, E_n. (b) Cumulative energy distribution. □: Smooth; △: rough.

fields for each flow case by projecting the instantaneous fluctuating velocity fields of a given ensemble onto the minimum number of leading POD modes required to capture 50 % of the TKE ($\langle u'^2 + v'^2 + w'^2 \rangle$) at $y = 0.15\delta$. The first 15 modes are required for the smooth-wall case while the first 16 modes are needed for the rough-wall case.

Figure 21(a) presents the low-order (large-scale) velocity field associated with the smooth-wall instantaneous realization in the x–z plane at $y = 0.15\delta$ presented in figure 5. The gross features of the original velocity field are clearly reflected in the low-order representation, particularly the low- and high-momentum regions and their associated extents in the streamwise and spanwise directions as well as their propensity to meander in the spanwise direction. Large-scale ejections of fluid ($v' > 0$) are also evident within the LMR while large-scale sweeps ($v' < 0$) are apparent in the HMR. These large-scale ejections and sweeps highlight the coherent RSS-producing motions collectively-induced by vortex organization in these flows. In contrast, the associated residual velocity field shown in figure 21(b) captures the smaller-scale features of the original velocity field, particularly the vortices that line the edges of the LMR and HMR as well as the more intermittent, yet intense, ejection and sweep events generated by these individual structures. Similar behaviour is noted in figures 21(c) and 21(d) which present the low-order and residual velocity fields associated with the original rough-wall velocity realization in the x–z plane at $y = 0.15\delta$ shown in figure 7. In particular, the large-scale characteristics of the identified LMR and HMR are captured in the large-scale field while the more intermittent smaller-scale turbulent events are evident in the residual field. This qualitative consistency between the smooth- and rough-wall large- and small-scale fields indicates that similar structural attributes are responsible for the, on average, 50 % of the TKE captured in each decomposition.

	Percentage contribution			
	Low-order		Residual	
Reynolds stress	Smooth	Rough	Smooth	Rough
$\langle u'^2\rangle^+$	69.0	68.0	31.0	32.0
$\langle v'^2\rangle^+$	12.9	11.2	87.1	88.8
$\langle w'^2\rangle^+$	31.4	32.3	68.6	67.7
$\langle u'v'\rangle^+$	64.3	57.3	35.7	42.7

TABLE 5. Percentage contributions of the low-order and residual velocity ensembles to the Reynolds stresses at $y = 0.15\delta$.

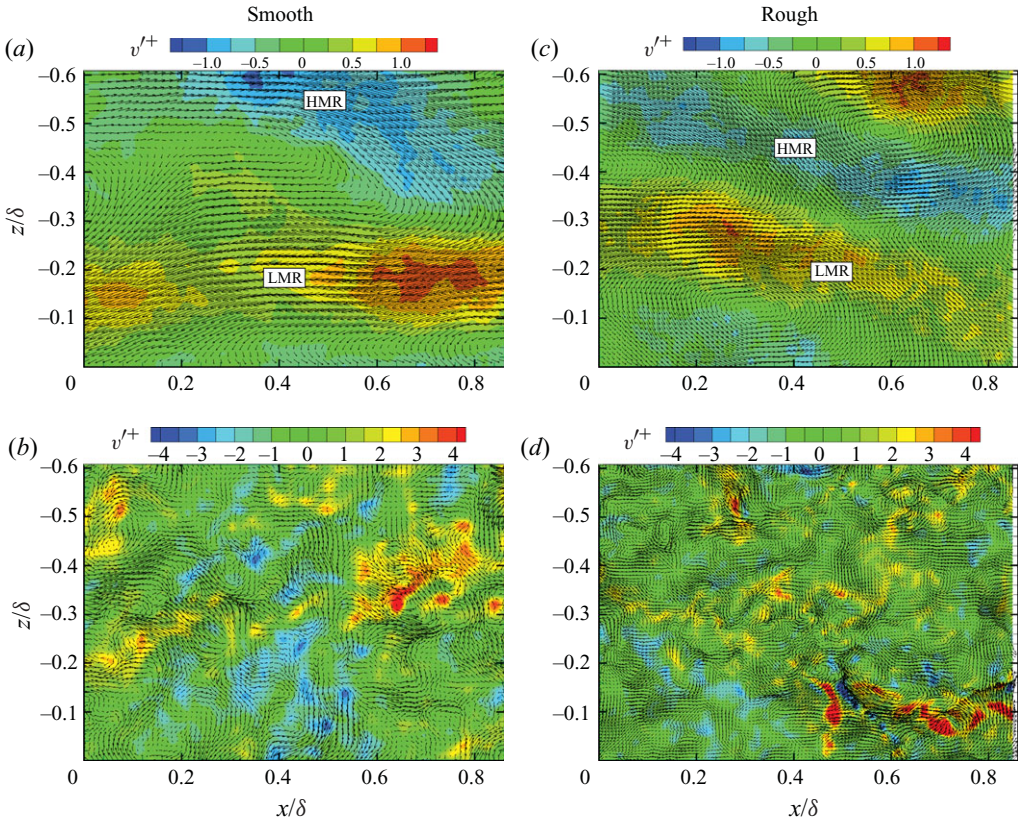

FIGURE 21. Low-order and residual representations of instantaneous fluctuating velocity fields from figures 5 and 7 in the x–z plane at $y = 0.15\delta$ for (a, b) smooth- (figure 5) and (c, d) rough-wall (figure 7) flow. In-plane velocity components (u'^+, w'^+) presented as vectors, out-of-plane component v'^+ as contours. Not every vector is shown for clarity.

As was done for the x–y POD analysis, the contributions of the low-order and residual velocity fields to the Reynolds normal and shear stresses at $y = 0.15\delta$ are calculated. Table 5 presents these results and large-scale flow features at $y = 0.15\delta$ are found embody a significant fraction of $\langle u'^2\rangle^+$, consistent with the POD analysis in the x–y plane. In contrast, a majority of $\langle v'^2\rangle^+$ and $\langle w'^2\rangle^+$ is attributable to the

smaller spatial scales, most significantly in the case of $\langle v'^2\rangle^+$. Finally, larger spatial scales are the dominant contributor in both flows to $\langle u'v'\rangle^+$, though these larger scales contribute slightly less in the case of roughness. This latter trend is again consistent with the smooth- and rough-wall POD analysis performed in the x–y plane.

Finally, the average spatial characteristics embodied in the low-order and residual velocity ensembles are assessed via spatial correlations. Figures 22(a) and 22(b) present two-point correlations of low-order streamwise velocity ($\rho_{u_Lu_L}$) in the x–z plane at $y=0.15\delta$ for flow over the smooth and rough surfaces, respectively. Of particular interest, $\rho_{u_Lu_L}$ is elongated in the streamwise direction and is bounded by regions of negative correlation in the spanwise direction. These patterns are consistent with the streamwise-elongated, spanwise-alternating LMRs and HMRs noted in instantaneous velocity realizations of both flows as well as the large-scale characteristics of ρ_{uu} computed from the original velocity fields at $y=0.15\delta$ (figure 9). This consistency is expected since the most energetic POD modes utilized in this reconstruction necessarily embody larger spatial scales. However, unlike the contour plots of ρ_{uu} that do not show an obvious shortening in streamwise extent (figure 9), the contour plots of $\rho_{u_Lu_L}$ reveal a substantial streamwise shortening in the presence of roughness. In contrast, the two-point correlations of residual streamwise velocity, $\rho_{u_Ru_R}$ (figures 22e and 22f), necessarily reflect the smaller-scale motions embodied in the higher-order POD modes as they are rather compact in both the streamwise and spanwise directions and regions of negative correlation surround the positive correlation peak. This arrangement is consistent with the spatial characteristics of small-scale wall-normal vortex cores in the x–z plane.

Figures 22(c) and 22(d) present one-dimensional profiles of $\rho_{u_Lu_L}$ in the streamwise and spanwise directions while figures 22(g) and 22(h) present similar profiles of $\rho_{u_Ru_R}$. These profiles facilitate comparison of the spatial extents of these large- and small-scale correlations for the smooth and rough cases. The spanwise extents of $\rho_{u_Lu_L}$ and $\rho_{u_Ru_R}$ are quite similar between the smooth and rough cases which is consistent with the similarity in the spanwise extent of ρ_{uu} computed from the original velocity fields of smooth- and rough-wall flow (figure 10). However, the streamwise extent of $\rho_{u_Lu_L}$ is reduced considerably ($\sim$25 %) in the presence of roughness, consistent with the reduced streamwise extent noted in the one-dimensional streamwise profiles of ρ_{uu} itself. In contrast, the streamwise extent of $\rho_{u_Ru_R}$ shows little sensitivity to roughness, indicating that the smaller scales of the flow are not appreciably altered by the roughness considered.

Large- and small-scale wall-normal velocity correlation coefficients, $\rho_{v_Lv_L}$ and $\rho_{v_Rv_R}$, are presented in figures 23(a, b) and 23(e, f) for flow over the smooth and rough surfaces at $y=0.15\delta$. Both cases of $\rho_{v_Lv_L}$ (smooth and rough) are elongated in the streamwise direction and flanked by weaker negative correlation regions in the spanwise direction, much like $\rho_{u_Lu_L}$. These patterns reflect the spanwise-alternating large-scale regions of ejections and sweeps noted in the instantaneous low-order velocity fields in the x–z plane (figures 21a and 21c). Interestingly, $\rho_{v_Lv_L}$ bears little resemblance to ρ_{vv} (figure 11), indicating that while ρ_{vv} embodies some larger-scale coherence in both the streamwise and spanwise directions, this coherence is secondary to that of the smaller scales. Indeed, $\rho_{v_Rv_R}$ is spatially compact in a manner consistent with the spatial characteristics of ρ_{vv}, indicative of the strong influence of smaller scales on the wall-normal velocity fluctuations. The spatial extents of $\rho_{v_Lv_L}$ and $\rho_{v_Rv_R}$ are compared via one-dimensional streamwise and spanwise profiles in figures 23(c, d) and 23(g, h), respectively. Similar to $\rho_{u_Lu_L}$ and $\rho_{u_Ru_R}$, the spanwise

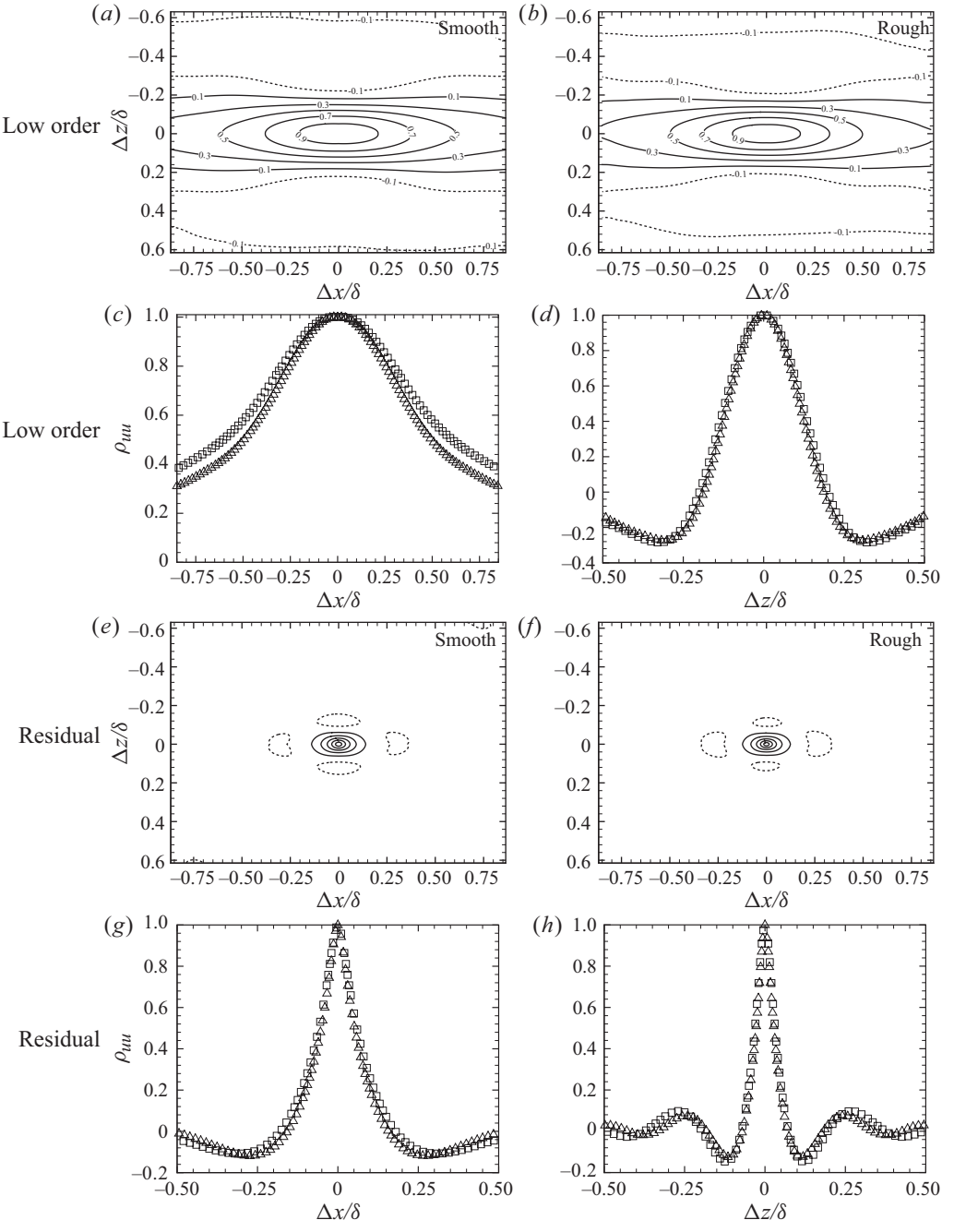

FIGURE 22. Streamwise velocity correlation coefficients of the (*a–d*) low-order ($\rho_{u_L u_L}$) and (*e–h*) residual ($\rho_{u_R u_R}$) contributions in the x–z plane at $y = 0.15\delta$ for smooth- and rough-wall flow. □: Smooth; △: rough.

extents of $\rho_{v_L v_L}$ and $\rho_{v_R v_R}$ are insensitive to roughness as the smooth and rough cases collapse well. However, the streamwise extent of $\rho_{v_L v_L}$ is reduced slightly in the presence of roughness while the streamwise extent of $\rho_{v_R v_R}$ shows little sensitivity to roughness. This slight streamwise shortening of $\rho_{v_L v_L}$ is consistent with the character

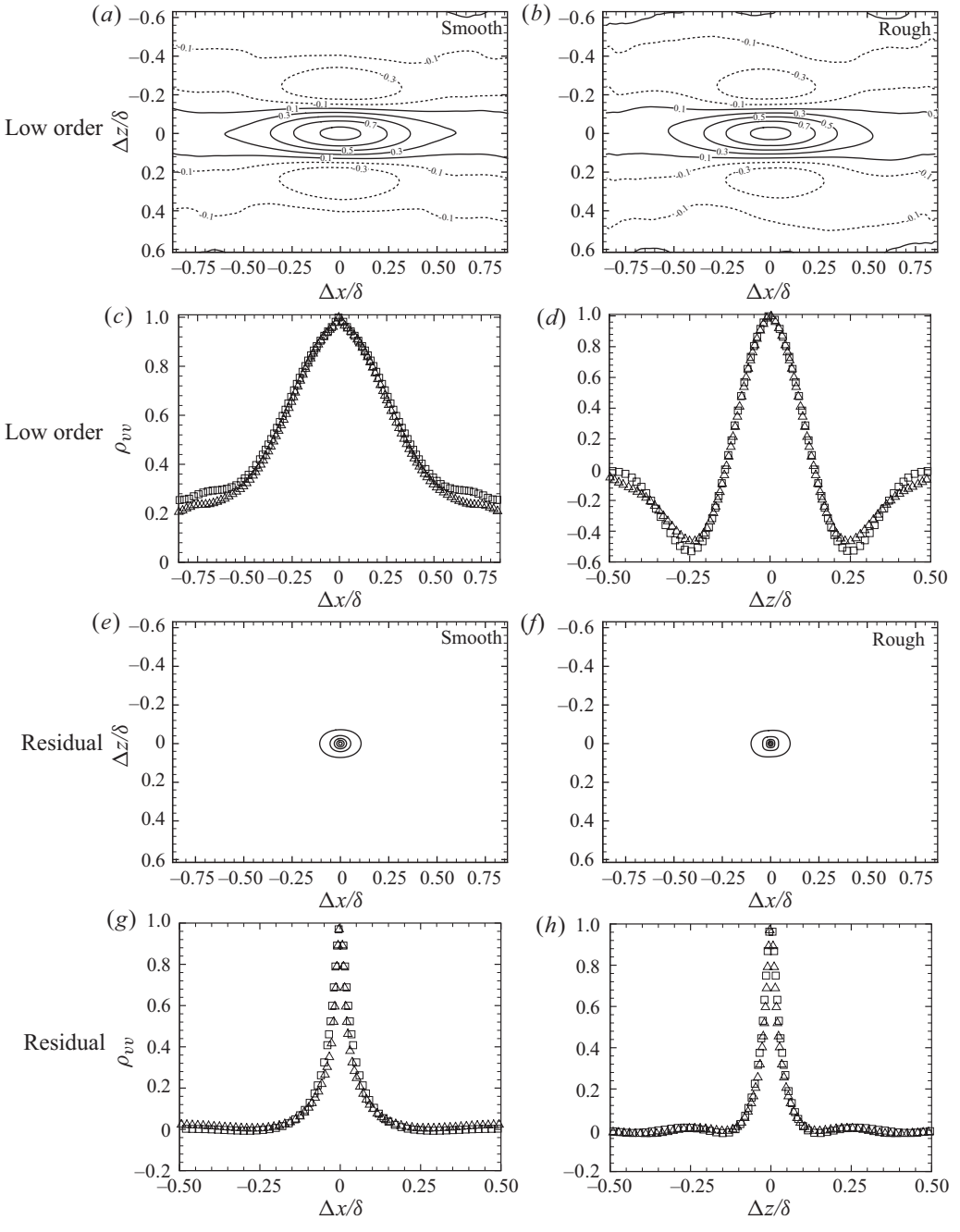

FIGURE 23. Wall-normal velocity correlation coefficients of the (*a–d*) low-order ($\rho_{v_L v_L}$) and (*e–h*) residual ($\rho_{v_R v_R}$) contributions in the x–z plane at $y = 0.15\delta$ for smooth- and rough-wall flow. □: Smooth; △: rough.

of $\rho_{u_L u_L}$ which further supports a roughness-induced modification of the larger streamwise spatial scales.

Finally, spanwise velocity correlation coefficients $\rho_{w_L w_L}$ and $\rho_{w_R w_R}$ at $y = 0.15\delta$ are presented in figure 24 for flow over the smooth and rough surfaces and comparable

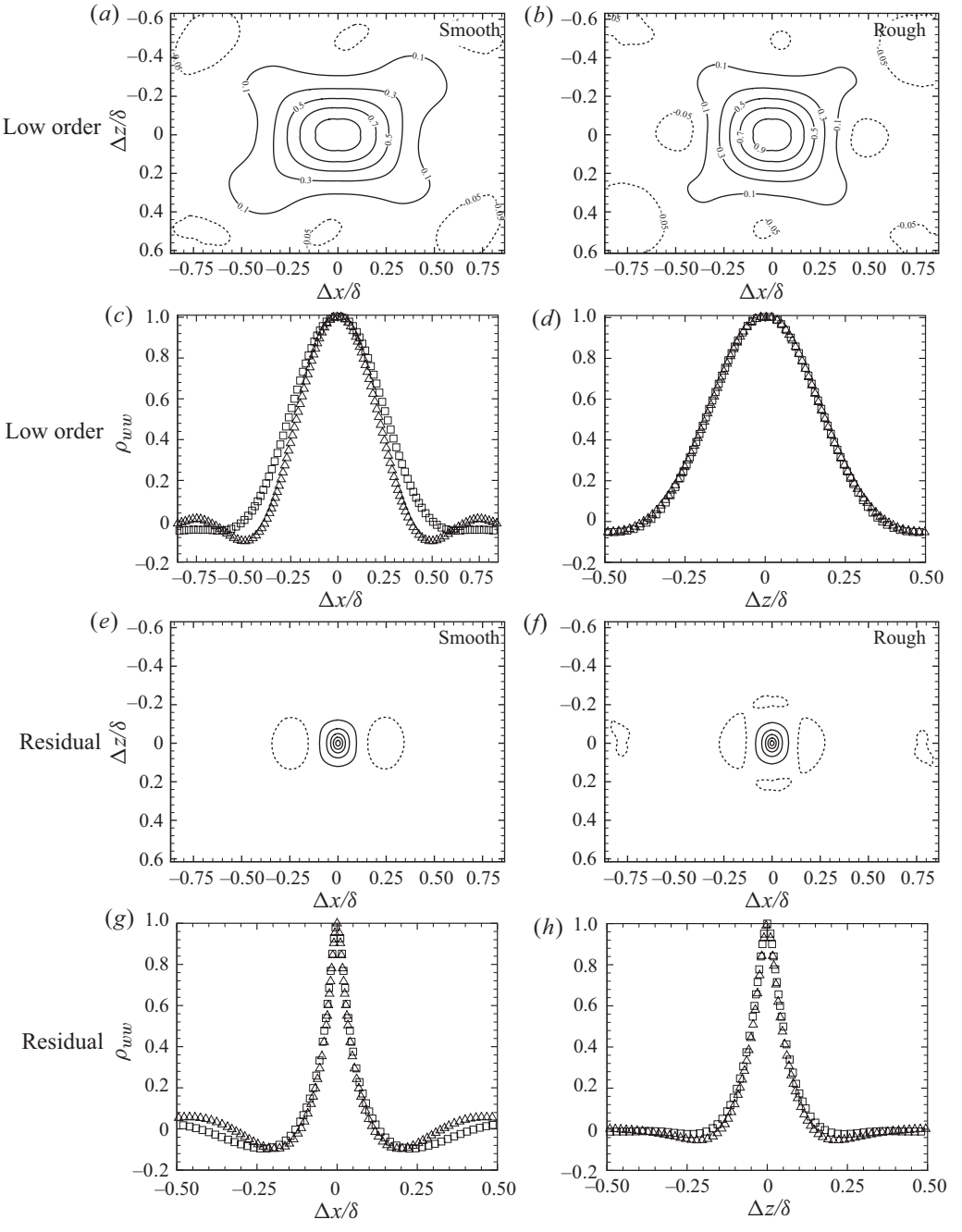

FIGURE 24. Spanwise velocity correlation coefficients of the (*a–d*) low-order ($\rho_{w_L w_L}$) and (*e–h*) residual ($\rho_{w_R w_R}$) contributions in the x–z plane at $y = 0.15\delta$ for smooth- and rough-wall flow. □: Smooth; △: rough.

streamwise and spanwise extents are noted in $\rho_{w_L w_L}$ as well as $\rho_{w_R w_R}$. The one-dimensional profiles of $\rho_{w_L w_L}$ and $\rho_{w_R w_R}$ in the spanwise direction show little sensitivity to roughness as the smooth and rough cases collapse. In contrast, the streamwise extent of $\rho_{w_L w_L}$ is reduced approximately 23 % in the presence of roughness, as was observed

for both $\rho_{u_L u_L}$ and $\rho_{v_L v_L}$. Further, the streamwise profile of $\rho_{w_L w_L}$ for the rough-wall flow falls below zero and rises again to achieve a secondary positive correlation peak. The absence of this behaviour in the smooth-wall case may be indicative of an enhanced spanwise meandering of these large-scale motions in the presence of the rough surface. Finally, the streamwise extent of $\rho_{w_R w_R}$ appears unaffected by roughness for smaller spatial separations, though a slight reduction in the location of the zero crossing is evident.

6. Summary and conclusions

The results presented highlight both strong similarities and important differences between the spatial structure of flow over a smooth wall and a highly irregular rough surface at $Re_\theta \approx 13\,000$. The instantaneous character of the flow inferred from two-dimensional PIV fields in the x–y plane and stereo PIV fields in the x–z plane at $y = 0.15\delta$ reveal clear imprints of outer-layer vortex organization – a well-established feature of smooth-wall turbulence. In particular, these instantaneous velocity realizations indicate that large-scale low- and high-momentum regions exist in both flows and that these large-scale features are quite energetic and embody a strong majority of the RSS. From a structural viewpoint, these large-scale features are interpreted to be the by-product of hairpin vortex packets, indicating that the structural foundation of smooth-wall flow is not appreciably altered by the roughness under consideration.

Similar qualitative consistency is also noted between the smooth- and rough-wall correlations of velocity and swirling strength which have been previously noted to embody definitive imprints of the underlying structure in smooth-wall flow. In particular, the streamwise-elongated yet inclined nature of ρ_{uu} in the x–y plane is maintained in the rough-wall flow as is the smaller-scale character of both ρ_{vv} and ρ_{ww}. Further, the spanwise-alternating, streamwise-elongated positive and negative correlation regions that mark ρ_{uu} in the wall-parallel plane at $y = 0.15\delta$ in smooth-wall flow are also observed in the rough-wall flow. As such, this evidence further supports the similarity in the structural foundations of the smooth- and rough-wall flows, particularly the existence of LMRs and HMRs that are linked to the presence of hairpin vortex packets. Despite these strong similarities, quantitative comparison of the smooth- and rough-wall correlations reveals some differences. In particular, the streamwise extents of ρ_{uu} as well as both $\rho_{\lambda_y \lambda_y}$ and $\rho_{\lambda_z \lambda_z}$ are reduced in the presence of roughness. Since the streamwise-elongated character of these correlations has been previously tied to the streamwise alignment of vortices into larger-scale packets (Tomkins & Adrian 2003; Christensen & Wu 2005), this reduction in streamwise extent is indicative of a commensurate reduction in the characteristic streamwise length scales of these larger-scale structures as inferred from these correlations. Interestingly, while the streamwise extent of ρ_{uu} is altered by roughness, its inclination angle is not.

Filtering of the velocity ensembles into larger- and smaller-scale fields via POD again reveals that the largest spatial scales tend to be most sensitive to roughness effects. Two-point correlations of the large-scale fields indicate the streamwise coherence of not only the u' auto-correlation to be significantly reduced by roughness but also the large-scale streamwise coherence of the v' and w' auto-correlations as well. These latter reductions in large-scale streamwise coherence were not notable in the full auto-correlations since these velocity components tend to be dominated by smaller scales. In contrast, the spanwise extents of these large-scale correlations are

unchanged in the presence of roughness. Spatial correlations of the small-scale velocity fields indicate strong insensitivity to roughness effects. Despite these differences, the contributions of the large- and small-scale features of the flow to the turbulent stresses are found to be similar irrespective of surface condition.

There are several possible explanations for the streamwise shortening of the larger turbulence scales by roughness as inferred from the correlations presented herein. These possibilities include a reduction in the streamwise spacing of consecutive vortices in vortex packets, a suppression of the vortex regeneration mechanism thought to be the impetus behind outer-layer vortex organization and/or an alteration of the spanwise meandering of these large-scale motions in the log layer. In this latter regard, Hutchins & Marusic (2007) used synthetic low-momentum regions to show that spanwise meandering of these motions can mask their true streamwise extent in ρ_{uu}. Thus, if roughness were to enhance this meandering compared to smooth-wall flow, a commensurate shortening of ρ_{uu} relative to the smooth-wall result would be expected. This trend is entirely consistent with the results presented herein. Alternatively, the results of Tomkins (2001), wherein a noted shortening of ρ_{uu} was reported just downstream of sparsely-spaced hemispheres in a turbulent boundary layer, indicate that the shortening of ρ_{uu} reported herein may also be due, at least in part, to isolated vortical structures generated by the roughness. The net impact of these isolated roughness-generated structures that probably scale with the roughness height k would be to reduce the streamwise extent of ρ_{uu} that is otherwise dominated by larger-scale outer-layer vortex organization in smooth-wall flow.

Finally, the observations of streamwise shortening of the larger spatial scales of the flow near the outer edge of the roughness sublayer by the specific irregular roughness considered herein are qualitatively similar to that noted in previous studies of more idealized three-dimensional roughness topographies (Krogstad & Antonia 1994; Volino *et al.* 2007). However, the degree of shortening observed is likely to be linked to the details of the roughness topography in question, as is evident when comparing the present results to those of Volino *et al.* (2007) for mesh roughness. Nevertheless, it appears that the three-dimensionality of the roughness in question is key to this reduction as recent studies of two-dimensional roughness report an increase in the characteristic streamwise scales of the flow well into the outer layer (see e.g. Volino *et al.* 2009).

This work was supported by the Air Force Office of Scientific Research under Grants FA9550-05-1-0043 and FA9550-05-1-0246 (Dr John Schmisseur, Programme Manager). The roughness sample studied was graciously loaned to us by Professor J. Bons of Ohio State University.

REFERENCES

Adrian, R. J., Christensen, K. T. & Liu, Z. C. 2000*a* Analysis and interpretation of instantaneous turbulent velocity fields. *Exp. Fluids* **29**, 275–290.

Adrian, R. J., Meinhart, C. D. & Tomkins, C. D. 2000*b* Vortex organization in the outer region of the turbulent boundary layer. *J. Fluid Mech.* **422**, 1–54.

Allen, J. J., Shockling, M. A., Kunkel, G. J. & Smits, A. J. 2007 Turbulent flow in smooth and rough pipes. *Phil. Trans. R. Soc.* A **365**, 699–714.

Bakken, O. M., Frogstad, P. A., Ashrafian, A. & Andersson, H. I. 2005 Reynolds number effects in the outer layer of the turbulent flow in a channel with rough walls. *Phys. Fluids* **17**, 065101.

Balakumar, B. J. & Adrian, R. J. 2007 Large- and very-large-scale motions in channel and boundary-layer flows. *Phil. Trans. R. Soc.* A **365**, 665–681.

Bandyopadhyay, P. R. & Watson, R. D. 1988 Structure of rough-wall turbulent boundary layers. *Phys. Fluids* **31**, 1877–1883.

Bons, J. P. 2002 St and C_f augmentation for real turbine roughness with elevated free stream turbulence. *J. Turbomach.* **124**, 632–644.

Bons, J. P., Taylor, R. P., McClain, S. T. & Rivir, R. B. 2001 The many faces of turbine surface roughness. *J. Turbomach.* **123**, 739–748.

Brown, G. L. & Thomas, A. S. W. 1977 Large structure in a turbulent boundary layer. *Phys. Fluids* **20**, S243–S252.

Carlier, J. & Stanislas, M. 2005 Experimental study of eddy structures in a turbulent boundary layer using particle image velocimetry. *J. Fluid Mech.* **535**, 143–188.

Cazemier, W., Verstappen, R. W. C. P. & Veldman, A. E. P. 1998 Proper orthogonal decomposition and low-dimensional models for driven cavity flows. *Phys. Fluids* **10** (7), 1685–1699.

Chong, M. S., Soria, J., Perry, A. E., Chacin, J., Cantwell, B. J. & Na, Y. 1998 Turbulence structures of wall-bounded shear flows found using DNS data. *J. Fluid Mech.* **357**, 225–247.

Christensen, K. T. & Adrian, R. J. 2001 Statistical evidence of hairpin vortex packets in wall turbulence. *J. Fluid Mech.* **431**, 433–443.

Christensen, K. T. & Wu, Y. 2005 Characteristics of vortex organization in the outer layer of wall turbulence. In *Fourth International Symposium on Turbulence and Shear Flow Phenomena*, Williamsburg, VA.

Colebrook, C. F. 1939 Turbulent flow in pipes with particular reference to the transition region between the smooth- and rough-pipe laws. *J. Inst. Civil Engng* **11**, 133–56.

Connelly, J. S., Schultz, M. P. & Flack, K. A. 2006 Velocity-defect scaling for turbulent boundary layers with a range of relative roughness. *Exp. Fluids* **40**, 188–195.

Delo, C. J., Kelso, R. M. & Smits, A. J. 2004 Three-dimensional structure of a low-Reynolds-number turbulent boundary layer. *J. Fluid Mech.* **512**, 47–83.

Falco, R. E. 1991 A coherent structure model of the turbulent boundary layer and its ability to predict Reynolds number dependence. *Phil. Trans. R. Soc. Lond.* A **336**, 103–129.

Flack, K. A., Schultz, M. P. & Shapiro, T. A. 2005 Experimental support for Townsend's Reynolds number similarity hypothesis on rough walls. *Phys. Fluids* **17**, 035102.

Flores, O., Jimenez, J. & del Alamo, J. C. 2007 Vorticity organization in the outer layer of turbulent channels with disturbed walls. *J. Fluid Mech.* **591**, 145–154.

Ganapathisubramani, B., Hutchins, N., Hambleton, W. T., Longmire, E. K. & Marusic, I. 2005 Investigation of large-scale coherence in a turublent boundary layer using two-point correlations. *J. Fluid Mech.* **524**, 57–80.

Ganapathisubramani, B., Longmire, E. K. & Marusic, I. 2003 Characteristics of vortex packets in turbulent boundary layers. *J. Fluid Mech.* **478**, 35–46.

Geers, L., Tummers, M. & Hanjalic, K. 2005 Particle imaging velocimetry-based identification of coherent structures in normally impinging multiple jets. *Phys. Fluids* **17**, 055105.

Guala, M., Hommema, S. E. & Adrian, R. J. 2006 Large-scale and very-large-scale motions in turbulent pipe flow. *J. Fluid Mech.* **554**, 521–542.

Head, M. R. & Bandyopadhyay, P. 1981 New aspects of turbulent boundary-layer structure. *J. Fluid Mech.* **107**, 297–338.

Holmes, P., Lumley, J. & Berkooz, G. 1996 *Turbulence, Coherent Structures, Dynamical Systerms and Symmetry*. Cambridge University Press.

Hutchins, N. & Marusic, I. 2007 Evidence of very long meandering features in the logarithmic region of turbulent boundary layers. *J. Fluid Mech.* **579**, 1–28.

Jimenez, J. 2004 Turbulent flow over rough wall. *Annu. Rev. Fluid Mech.* **36**, 173–196.

Karlsson, R. I. 1980 Studies of skin friction in turbulent boundary layers on smooth and rough walls. PhD thesis, Department of Allied Thero and Fluid Dynamics, Chalmers University of Technology, Göteborg, Sweden.

Keirsbulck, L., Labraga, L., Mazouz, A. & Tournier, C. 2002 Surface roughness effects on turbulent boundary layer structures. *J. Fluids Engng* **124**, 127–135.

Kim, K. C. & Adrian, R. J. 1999 Very large-scale motion in the outer layer. *Phys. Fluids* **11**, 417–422.

Kostas, J., Soria, J. & Chong, M. 2005 A comparison between snapshot POD analysis of PIV velocity and vorticity data. *Exp. Fluids* **38**, 146–160.

KROGSTAD, P. A. & ANTONIA, R. A. 1994 Structure of turbulent boundary layers on smooth and rough walls. *J. Fluid Mech.* **277**, 1–21.

KROGSTAD, P. A. & ANTONIA, R. A. 1999 Surface roughness effects in turbulent boundary layers. *Exp. Fluids* **27**, 450–460.

KROGSTAD, P. A., ANTONIA, R. A. & BROWNE, L. W. B. 1992 Comparison between rough and smooth-wall turbulent boundary layers. *J. Fluid Mech.* **245**, 599–617.

KUNKEL, G. J. & MARUSIC, I. 2006 Study of the near-wall-turbulent region of the high-Reynolds-number boundary layer using an atmospheric flow. *J. Fluid Mech.* **548**, 375–402.

LEE, S. H. & SUNG, H. J. 2007 Direct numerical simulation of the turbulent boundary layer over a rod-roughened wall. *J. Fluid Mech.* **584**, 125–146.

LIGRANI, P. M. & MOFFAT, R. J. 1986 Structure of transitionally rough and fully rough turbulent boundary layers. *J. Fluid Mech.* **162**, 69–98.

LIU, Z., ADRIAN, R. J. & HANRATTY, T. J. 2001 Large-scale modes of turbulent channel flow: transport and structure. *J. Fluid Mech.* **448**, 53–80.

MEINHART, C. D. 1994 Investigation of turbulent boundary-layer structure using particle-image velocimetry. PhD thesis, Department of Theoretical and Applied Mechanics, University of Illinois at Urbana-Champaign, IL.

MEINHART, C. D. & ADRIAN, R. J. 1995 On the existence of uniform momentum zones in a turbulent boundary layer. *Phys. Fluids* **7**, 694–696.

NAKAGAWA, S. & HANRATTY, T. J. 2001 Particle image velocimetry measurements of flow over a wavy wall. *Phys. Fluids* **13** (11), 3504–3507.

NATRAJAN, V. K. & CHRISTENSEN, K. T. 2006 The role of coherent structures in subgrid-scale energy transfer within the log layer of wall turbulence. *Phys. Fluids* **18**, 065104.

NATRAJAN, V. K., WU, Y. & CHRISTENSEN, K. T. 2007 Spatial signatures of retrograde spanwise vortices in wall turbulence. *J. Fluid Mech.* **574**, 155–167.

NIKURADSE, J. 1933 Laws of flow in rough pipes. *Tech. Mem.* No. 1292. NACA.

PANTON, R. L., ed. 1997 *Self-Sustaining Mechanisms of Wall Turbulence*. Computational Mechanics Publications.

RAUPACH, M. R. 1981 Conditional statistics of reynolds stress in rough-wall and smooth-wall turbulent boundary layers. *J. Fluid Mech.* **108**, 363–382.

RAUPACH, M. R., ANTONIA, R. A. & RAJAGOPALAN, S. 1991 Rough-wall turbulent boundary layers. *Appl. Mech. Rev.* **44**, 1–25.

ROBINSON, S. K. 1991 Coherent motions in the turbulent boundary layer. *Annu. Rev. Fluid Mech.* **23**, 601–39.

SABOT, J., SALEH, I. & COMTE-BELLOT, G. 1977 Effects of roughness on the intermittent maintenance of Reynolds shear stress in pipe flow. *Phys. Fluids* **20, Pt II** (10), S150–S155.

SIROVICH, L. 1987 Turbulence and the dynamics of coherrent structures. Part 1. Coherent structures. *Q. Appl. Math.* **45**, 561.

SMITH, C. R. 1984 A synthesized model of the near-wall behaviour in turbulent boundary layers. In *Proceedings of the 8th Symposium on Turbulence* (ed. J. Z. G. Patterson), pp. 333–364. University of Missouri-Rolla, Rolla, MO.

SMITH, C. R., WALKER, J. D. A., HAIDARI, A. H. & SOBRUN, U. 1991 On the dynamics of near-wall turbulence. *Phil. Trans. R. Soc. Lond.* A **336**, 131–175.

SOLOFF, S. M., ADRIAN, R. J. & LIU, Z.-C. 1997 Distortion compensation for generalized stereoscopic particle image velocimetry. *Meas. Sci. Technol.* **8**, 1441–1454.

STANISLAS, M., PERRET, L. & FOUCAT, J.-M. 2008 Vortical structures in the turbulent boundary layer: a possible route to a universal representation. *J. Fluid Mech.* **602**, 327–382.

TACHIE, M. F., BERGSTROM, D. J. & BALACHANDAR, R. 2000 Rough wall turbulent boundary layers in shallow open channel flow. *J. Fluids Engng* **122**, 533–541.

TACHIE, M. F., BERGSTROM, D. J. & BALACHANDAR, R. 2003 Roughness effects in low-Re_h open-channel turbulent boundary layers. *Exp. Fluids* **35**, 338–346.

TOMKINS, C. D. 2001 The structure of turbulence over smooth and rough walls. PhD thesis, University of Illinois at Urbana-Champaign, IL.

TOMKINS, C. D. & ADRIAN, R. J. 2003 Spanwise structure and scale growth in turbulent boundary layers. *J. Fluid Mech.* **490**, 37–74.

Volino, R. J., Schultz, M. P. & Flack, K. A. 2007 Turbulence structure in rough- and smooth-wall boundary layers. *J. Fluid Mech.* **592**, 263–293.

Volino, R. J., Schultz, M. P. & Flack, K. A. 2009 Turbulence structure in a boundary layer with two-dimensional roughness. *J. Fluid Mech.* **635**, 75–101.

Wieneke, B. 2005 Stereo-PIV using self-calibration on particle images. *Exp. Fluids* **39**, 267–280.

Wu, Y. 2008 Experimental investigation of highly irregular roughness effects in wall turbulence. PhD thesis, University of Illinois at Urbana-Champaign, IL.

Wu, Y. & Christensen, K. T. 2006 Population trends of spanwise vortices in wall turbulence. *J. Fluid Mech.* **568**, 55–76.

Wu, Y. & Christensen, K. T. 2007 Outer-layer similarity in the presence of a practical rough-wall topography. *Phys. Fluids* **19**, 085108.

Zhou, J., Adrian, R. J., Balachandar, S. & Kendall, T. M. 1999 Mechanisms for generating coherent packets of hairpin vortices in channel flow. *J. Fluid Mech.* **387**, 353–396.